Measurements and Interpretation of Crude Oil-Water/Brine Dynamic Interfacial Tension at Subsurface Representative Conditions

Kaiqiang Zhang[1,2], Apostolos Georgiadis[1,3] and J. P. Martin Trusler[1]*

[1]Department of Chemical Engineering, Imperial College London, South Kensington Campus, London SW7 2AZ, United Kingdom

[2]Institute of Energy, Peking University, Beijing 100871, PR China

[3]Shell Global Solutions International B.V., 1031 HW Amsterdam, The Netherlands

*Corresponding author: m.trusler@imperial.ac.uk (J. P. M. Trusler)

Abstract

Interfacial tensions (IFTs) between crude oil and water or brine systems are critically important in many processes. Exhibited dynamic behavior often remains poorly studied and requires in-depth analysis. In this study, 27 series of dynamic IFT measurements were conducted for three different crude oils in combination with three different aqueous phases (pure water and two synthetic reservoir brines) at temperatures of 298.15, 343.15 and 393.15 K and pressures up to 30 MPa. This study provides a large database of crude oil-water/brine IFTs encompassing reservoir conditions of temperature and pressure. Specific effects of temperature, pressure, and fluid composition on the crude oil-water and oil-brine IFTs were evaluated. The dynamic evolution of the IFT between the crude oils and aqueous phases was categorized according to typical relationships observed. The most commonly observed evolution was an initial rapid decline in IFT, over a period of 100 to 1,000 s, followed by levelling off at a nearly-constant long-term value. However, in certain cases, the initial rapid decline was followed by a broad minimum and a subsequent slow increase towards a nearly-steady long-time value. In either case, the initial decline is described by a simple model based on diffusion of surface-active components in the oil and their subsequent adsorption at the interface. The longer-term behavior may be further attributed to a combination of saturation, rearrangement and dissolution of the surface-active components.

Keywords: dynamic interfacial tension; crude oil; reservoir conditions; diffusion model; surface-active component.

Introduction

Interfacial properties are of great importance in nature and in a host of industrial processes, such as oil/gas extraction and geological carbon storage [1,2]. As an important interfacial property quantitatively indicating complex interfacial interactions, an accurate determination of interfacial tension (IFT) is a critical prerequisite for many engineering and scientific endeavors [3,4]. From a thermodynamic perspective, the IFT is the partial derivative of the Gibbs free energy with respect to the interfacial area under conditions of constant temperature and pressure [5]. Given its wide significance, abundant research has been dedicated and determination methods applied are diverse both experimentally and in models [6–8]. IFTs can be experimentally measured by different means applicable over different, partly overlapping value ranges. These include common approaches such as the spinning drop method, the Du Noüy ring or Plate method, and axisymmetric drop shape analysis (ADSA) technique under either the pendant, standing or sessile drop arrangements [9–11]. IFTs can also be predicted by, for instance, the parachor model, gradient theory, and density functional theory [12–14]. Among the different experimental methods, the ADSA technique for the pendant/standing drop is a versatile method which has been widely applied for the IFT measurements also at high-pressure and high-temperature conditions [15–18]. Originally, IFTs were determined by photographing a pendant drop and measuring the drop dimensions from the negative films [19]. Later, the ADSA technique was developed to accurately determine the IFT by matching the shape profile of a pendant/standing drop with the analytical profile obtained by numerical integration of the Young–Laplace equation [15]. In the literature, the ADSA technique for the pendant/standing drop case has been employed to measure the IFTs of the various liquid and gas systems at a wide range of temperatures and pressures [16,18,20,21].

In relation to the systems of interest of this study, a number of experimental IFT studies have been reviewed. Key literature data of pure hydrocarbons and synthetic hydrocarbon mixtures-water/brine IFT measurements are summarized and listed in Table 1, most of which were focused on the temperature and pressure effects on the IFTs. In 1953, Hassan et al. measured the IFTs of C_3H_8/*n*-C_5H_{12}/*n*-C_6H_{14}/*n*-C_8H_{18}/*i*-C_8H_{18}–water systems at temperatures of 299.15 to 355.15 K and pressures up to 20.7 MPa by using the pendant drop method [22]. They found a slight decrease of the IFT with increasing pressure at constant temperature and a larger decrease with temperature at constant pressure. After that, numerous studies have been conducted to investigate the temperature and pressure effects on the hydrocarbons-water/brine IFTs. Aveyard and Haydon (1965) found the IFTs of a series of normal alkane–water systems were decreased with temperature [23]. Jennings Jr. et al. (1967) conducted IFT measurements for the $C_{10}H_{22}$–water system by using the pendant drop methods at temperatures of 298.15–449.15 K and pressures up to 82.8 MPa [24]. Generally, the measured $C_{10}H_{22}$–water IFTs were found to slightly increase with pressure but

substantially decrease with temperature. The effect of temperature on the IFTs was found to be much greater than that of pressure. McCaffery (1972) performed IFT measurements for the C_8H_{18}/$C_{12}H_{26}$-water systems at wide temperature range of 298.15–433.15 K and pressures from ambient to 68.9 MPa. Their measured IFTs were also found to be follow the same relationship with pressure and temperature [25]. Similar findings were obtained for the crude oil-water and oil-brine studies as well, covering both light and heavy crudes [26–33]. Although the temperature and pressure effects on the IFTs of crude oil/synthetic hydrocarbon-water/brine systems have been investigated for many years, the conclusions are not in consensus. As demonstrated in Table 1, most previous studies used synthetic hydrocarbons to represent the oil phase with crude oil samples being less reported and studied, partly owing to their challenging dynamic behavior and associated difficulty in interpreting the behavior of such systems.

Table 1. Previous studies for the interfacial tension of crude oil/synthetic hydrocarbon-water/brine systems

Oil phase	**Aqueous phase**	***T* (K)**	***P* (MPa)**	**Year**	**Ref.**
C_3H_8/C_5H_{12}/C_6H_{14}/*n*-C_8H_{18}/*i*-C_8H_{18}	water	299.15–355.15	0.1–20.7	1953	[22]
C_5H_{12}/C_6H_{14}/C_7H_{16}/C_8H_{18}/$C_{10}H_{22}$/$C_{12}H_{26}$/$C_{14}H_{30}$/$C_{16}H_{34}$	water	293.15–313.15	0.1	1965	[23]
$C_{10}H_{22}$	water	298.15–449.15	0.1–82.8	1967	[24]
C_8H_{18}/$C_{12}H_{26}$	water	298.15–433.15	0.1–68.9	1972	[25]
C_6H_{14}/C_8H_{18}/	water	303.15	0.1–150	1977	[26]
C_8H_{18}/$C_{12}H_{26}$	water, brines	296.45–449.85	0.1–82.74	1988	[30]
C_6H_{14}/C_8H_{18}/$C_{10}H_{22}$/$C_{12}H_{26}$/$C_{14}H_{30}$/$C_{16}H_{34}$	water, brines	298.15–353.15	0.1–30	1996	[27]
C_5H_{12}/C_6H_{14}/C_7H_{16}/C_8H_{18}/C_9H_{20}/$C_{10}H_{22}$/$C_{11}H_{24}$/$C_{12}H_{26}$/$C_{13}H_{28}$/$C_{14}H_{30}$/$C_{16}H_{34}$	water	295.15	0.1	1997	[31]
C_6H_{14}/C_7H_{16}/C_8H_{18}/C_9H_{20}/$C_{10}H_{22}$/$C_{11}H_{24}$/$C_{12}H_{26}$	water	283.15–333.15	0.1	2001	[28]
$C_{10}H_{22}$	water, brine	298.15	0.69–31.05	2005	[29]
crude oil	water, solutions	296.5–331	20.7	2005	[32]

Oil phase	Aqueous phase	*T* (K)	*P* (MPa)	Year	Ref.
	containing $NaCl/CaCl_2$				
heavy crude oil	solutions containing $NaCl/CaCl_2$	298.15–363.15	0.1–17.23	2014	[33]
acidic crude oil	solutions containing $MgCl_2/CaCl_2/MgSO/Na_2SO_4/CaSO_4/NaCl/KCl$	313.15	0.1	2014	[34]
light crude oil	water	303.15, 313.15 323.15, 333.15	0.1	2018	[35]

In addition to the temperature and pressure effects, the fluid composition of both oil and aqueous phases is a driving factor affecting IFTs. Goebel and Lunkenheimer (1997) used the Du Noüy ring method based on the automatic Lauda tensiometer to measure IFTs of eleven hydrocarbons–water systems at ambient conditions [31]. The effects of surface-active components (SACs) on the hydrocarbon–water systems were studied. They purified the hydrocarbon phase by shaking the sample with water and removed the formed interface. With increased number of purification cycles, the hydrocarbon–water IFTs were found to increase. For example, the *n*-$C_{10}H_{22}$–water IFTs increased from approximately 42 mN/m to almost 54 mN/m after six purification cycles. Zeppieri et al. (2001) measured seven hydrocarbon–water systems by using the drop shape analysis technique with a numerical method based on a fourth-degree spline interpolation of the drop profile. They found that in comparison with light hydrocarbons, heavier hydrocarbons usually have higher IFTs against water [28]. Recently, Perles et al. (2018) measured dynamic crude oil–water IFTs by using the pendant drop tensiometer at four different temperatures of 303.15–333.15 K and ambient pressure [35]. They also studied the interfacial rheology based on the oscillatory pendant drop technique (dilatational rheology). For the water–oil interface, the viscous and elastic moduli of the interfacial film were found to increase with time from the creation of the drop, and also with temperature increase. Although the authors investigated the interfacial rheology corresponding to the IFTs at different temperatures, specific analysis of the dynamic IFT evolution was not assessed. The brine composition effect is dependent on both ionic species and concentration. Lashkarbolooki et al. (2014) compared several common monovalent and divalent-salt solutions against a crude oil and found the salt-induced IFT reductions followed

the order of $MgCl_2$ > $CaCl_2$ > $MgSO_4$ > Na_2SO_4 > $CaSO_4$ > NaCl > KCl [34]. Starting from low concentrations, addition of these common salts resulted in significant IFT reduction but, with increasing concentration, this trend was found to reverse. Therefore, an optimum salt concentration exists at which the IFT is minimized [33]. Nevertheless, few previously reported studies have been found to investigate dynamic IFTs between crude oil and water/brines.

The present work is distinguished from previous studies in several important respects. First, it is a component of a wider Digital Rocks research program, which encompasses the same set of well-characterized reservoir fluids in conjunction with assessable porous media, studied by a wide range of methods to better understand and predict multiphase flow in the subsurface. Within this context, previous communications present key findings relevant to pore-scale flow [36,37], as well as associated fluid characterization and wettability simulation results [38,39]. Second, unlike previous studies, we include a detailed compositional analysis of the crude oils studied, based on bespoke two-dimensional GC analyses from which key component classes are identified by both carbon number and chemical family (see Fig. S1 in the Supporting Information). A third distinguishing feature of the present study is its scope: a total of 27 series of dynamic IFT tests were conducted for three distinct crude oils, selected based on their wide range of wetting effects assessed in core floods elsewhere, given the aliases Agen, Baring and Capita. These were measured against pure water and two representative brines, designated here as sandstone and carbonate brines, respectively. Isotherms measured included 298.15, 343.15 and 393.15 K, at pressures up to 30 MPa, using the ADSA technique for the standing drop arrangement of oil drops in a bulk aqueous phase. The dynamic crude oil–water and crude oil-brine IFT data were distinguished into periods of short-term diffusion-control and long-term relaxation, modeling the apparent interfacial tension as a function of time for newly created drops at each state point. The full dataset for the three crude oil-water and crude oil-brine IFTs at high-pressure high-temperature reservoir conditions are provided. Moreover, effects of temperature, pressure, and fluid compositions on the crude oil-water and crude oil-brines IFTs are evaluated. The experimental workflow and modelling interpretation presented here provides a basis and opportunity for interpreting the dynamic behavior of oil-water and oil-brines IFT at representative reservoir conditions.

Experimental section

Materials

The three different crude oil samples used in this study (stock tank liquids: Agen, Baring, and Capita) were provided by Shell as part of the Digital Rocks joint research program. These have been identified as representative fluids covering a wide range of wetting behavior observed in core-floods. The crude oils were homogenized by centrifugation, separating out

water and solids, prior to being characterized. Their physical properties are listed in Table 2, along with TAN, TBN and SARA analyses. The composition of the oils was also investigated at Shell by two-dimensional gas chromatography and the results of those analyses are presented in Fig. S1 of the Supplementary Materials. The figure illustrates the relative abundance of components ranging up to carbon number 35 for several identified molecular classes. These data were the basis of a surrogate fluid model previously developed including an articulated SAC composition [57]. On the basis of the physical properties, it is apparent that the three samples are light and medium crude oils that can be effectively recovered by conventional means, including waterflooding.

Table 2. Physical properties of crude oils used in this study, where ρ is density and η is dynamic viscosity at T = 293.15 K and P = 0.1 MPa, TAN and TBN are the total acid number and total basic nitrogen, respectively, and W is the Amott wettability index. These were determined by methods equivalent to ASTM D664, and ASTM D2896, respectively. SARA analysis was performed according to ASTM D2007.

Oil sample	ρ ($g \cdot cm^{-3}$)	η (mPa·s)	TAN ($mgKOH \cdot g^{-1}$)	TBN ($mg \cdot kg^{-1}$)	W	SARA analysis (wt.%)			
						Sat.	Aro.	Res.	Asp.
Agen	0.9347	88.4	1.37	320	0.34	37.27	48.45	14.21	0.07
Baring	0.8339	4.87	0.07	83.9	0.46	58.45	36.92	4.36	0.28
Capita	0.8592	9.47	0.09	270.6	0.58	44.00	44.00	9.69	2.31

To cover a range of aqueous phases, pure deionized and degassed water (electrical resistivity > 18 MΩ·cm at 298.15 K) and two synthetic reservoir brines, characteristic of sandstone and carbonate formations, were used. The brines were synthesized in the lab and their compositions are detailed in Table 3.

Table 3. Compositions of 'sandstone' and 'carbonate' brines used in this study (mass concentration at T = 298.15 K).

Ion	Sandstone brine ($g \cdot L^{-1}$)	Carbonate brine ($g \cdot L^{-1}$)
Na^+	4.267	49.898
K^+	7.238	0.000
Ca^{2+}	0.301	14.501
Mg^{2+}	0.024	3.248
Cl^-	13.744	111.812
SO_4^{2-}	0.000	0.234
HCO_3^-	0.000	0.162

Interfacial Tension Measurement

Apparatus. Fig. 1 is a schematic diagram of the apparatus used to carry out IFT measurements at high-pressure and high-temperature conditions, using the ADSA technique

for the standing oil drop arrangement. A detailed description of this apparatus has been given elsewhere [40] and here we provide only a summary. The main element of the measurement system is a high-pressure view cell made from grade 12 titanium alloy. The cell was fitted with axially opposed Poulter-type sapphire windows, and the maximum operating pressure and temperature were 50 MPa and 473.15 K, respectively. Four pressure ports were provided and two of these permitted capillaries of 1.6 mm o.d. to pass into the interior of the cell; one, entering from above for creating pendant drops and the other, entering from below, for standing drops. The other ports allowed filling and emptying of the cell. In this work, oil was injected through the lower capillary to form standing drops surrounded by bulk water or brine. This capillary was fed by a small stainless-steel vessel, which was used to store the crude oil during an experiment. Water was injected into the bottom of the storage vessel from a high-pressure pump to displace oil into the view cell. A system of two high-pressure syringe pumps

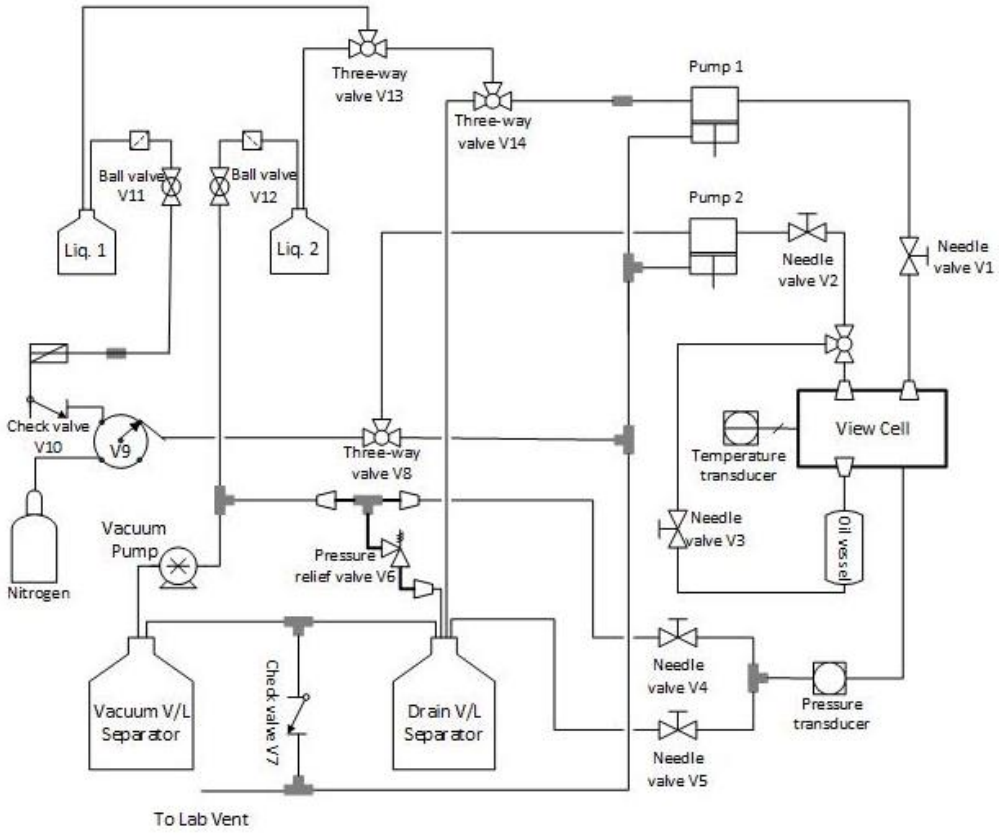

Figure 1. Schematic diagram of high-temperature high-pressure interfacial properties apparatus

(Quizix Q5000 series, Chandler Engineering) with wetted parts of Hastelloy C276 was used to inject water into the storage vessel and either water or brine into the view cell. To minimize dead volume and maintain corrosion resistance, titanium tubing of 1.6 mm o.d. × 0.5 mm i.d. was used for all connections. The imaging system comprised a CCD camera (Remé-Hart F4 Series FireWire, 100-12-F4) with a resolution of 659 x 494 pixels, fitted with a zoom lens

(Moritex ML-MC75HR, 75 mm, F3.8-16, x0.18-x0.38). Back illumination was provided by an adjustable LED light source fitted with a diffuser. To maintain axial alignment, the camera, view cell and light source were all mounted on an optical rail. A calibrated platinum resistance thermometer was inserted into an axial hole bored in the wall of the IFT cell and a pressure transducer was located in the tubing external to the IFT cell. The standard uncertainties for the temperature and pressure measurements were 0.05 K and 0.035 MPa, respectively.

Data analysis and calibration. The IFT γ was determined from the drop images by ADSA as implemented in commercial software (*DROPimage Advanced*, Ramé-Hart Instrument Co.). In this analysis, the drop image is matched with a theoretical profile obtained by numerical integration of the Young–Laplace equation. The results are expressed in terms of the measured radius of curvature at the apex of drop, R_0, and the Bond number β such that,

$$\gamma = \Delta\rho \cdot g R_0^2 / \beta \quad (1)$$

where $\Delta\rho$ is the density difference between the two fluids and g = 9.81 m s^{-2} is the gravitational acceleration.

An accurate IFT determination is contingent upon the accuracy of both the radius of curvature, the Bond number and the density difference. In this work, the imaging system was calibrated against a pair of standards which were a sphere and a cylinder both of diameter (4.000 ± 0.001) mm. The calibration tool was placed in the view cell as close to the capillary as possible, where the aspect ratio of the sphere and/or the diameter of the cylinder could be directly measured through *DROPimage Advanced*. A calibration is considered to be qualified as long as the aspect ratio is in the range of 0.9985-1.0015 and/or the cylinder diameter is (4.000 ± 0.001) mm. In this study, the captured aspect ratio and diameter are 0.9995 and 4.000 mm, respectively. The calibration was repeated after any change in the adjustment the camera lens. It should be noted that the calibration was conducted in the air, while the IFT measurements in this study were performed with water or brine in the cell. The difference in refractive index between air and the water/brine required application of a correction to the measured IFT [41] which, in this work, ranged up to approximately 4%.

In relation to the density difference, the oil and aqueous phases were treated as immiscible fluids. The density of pure water was obtained from the NIST Standard Reference Databases 23 [42] and the density of brine was calculated from model of Al Ghafri et al. [43,44]. We measured the crude oil densities at the relevant temperature and pressure conditions as detailed in the next section.

Experimental procedure. Prior to each IFT series, the entire system was cleaned with hexane, isopropanol, water, and flushed with helium in sequence, repeated several times. The system was also thoroughly leak-tested with both water and helium over the whole pressure

range. After cleaning and leak testing, the IFT cell was evacuated and then filled with water or brine to the initial target pressure at the each isotherm. Since hydrostatic equilibrium was attained much faster than thermal equilibrium, each group of IFT measurements was conducted at a fixed temperature with increasing pressure. After the system pressure and temperature stabilized, crude oil drops were created by injecting oil into the cell through the bottom capillary. Before measuring each new drop, at least three drops were introduced into the vessel to ensure the following one being measured would be consistently prime. The image acquisition commenced within approximately 2 seconds after each oil drop was formed. For every state point, at least three drops were measured, each studied for at least 1800 s at T = 298.15 K and 6000 s at T = 343.15 and 393.15 K. The pressure of the cell was adjusted by discharging or injecting water through the syringe pump operating in constant-pressure mode. At least 15 min was allowed to ensure that the system reached equilibrium after setting a new pressure. Overall, 27 series of dynamic IFT tests were carried out for the crude oils Agen, Baring and Capita against water and two brines (sandstone and carbonate) at temperatures of 298.15, 343.15, 393.15 K and pressures up to 30 MPa. The full dataset is shown in Figures S1–S3 of the Supplementary Material.

As discussed by Lv et al. [40], the overall combined standard uncertainty includes contributions from the uncertainties of the temperature and pressure, the density difference between the two phases and the repeatability of the measurements. In the present case, these terms combined to give a standard relative uncertainty of 2%.

Density Measurement

The oil density measurement was carried out with a high-pressure vibrating-tube densimeter (VTD, Anton-Paar model DMA HP), which was rated to 473.15 K and 140 MPa. The VTD was fitted with U-shaped Hastelloy vibrating-tube with internal volume of approximately 2 mL. The pressure and temperature of the injected fluid in the VTD were controlled by means of a high-pressure syringe pump and an oven, respectively. The in-situ temperature of the VTD was monitored by a small platinum resistance thermometer (PRT) capsule inserted into the cellblock and the pressure was obtained from a sensor attached to the syringe pump.

The oil density was obtained from the measured period of oscillation τ by means of the following seven-parameter physical model [45]:

$$\rho = \frac{(\rho_{\mathrm{M}} / S_{00})}{(1+\alpha_{\mathrm{V}} t + \beta_{\mathrm{V}} p)}\left[\left(\frac{\tau}{\tau_{00}(1+\varepsilon_{\tau 1} t + \varepsilon_{\tau 2} t^2)}\right)^2 (1+\beta_\tau p) - 1\right]. \quad (2)$$

Here, t is temperature in degrees Celsius, p is pressure, ρ_{M} is the (nominal) density of the tube material, S_{00} is a scale parameter, α_V and β_V are the temperature and pressure coefficients of

the tube internal volume, τ_{00} is the vacuum period at t = 0°C, $\varepsilon_{\tau 1}$ and $\varepsilon_{\tau 2}$ are the first and second temperature coefficients of the vacuum period, and β_τ is a pressure coefficient. In this study, we applied the constraint β_V = -3.87 β_τ, leaving six adjustable parameters which were determined by means of calibration with vacuum and water. The calibration measurements were carried out at temperatures up to 448.15 K and over the full working pressure range up to 60 MPa. The six adjustable parameters were obtained by fitting the measured periods in water making use of densities calculated from IAPWS equation of state [46]. The density deviations for the calibration data are shown in Fig. 2.

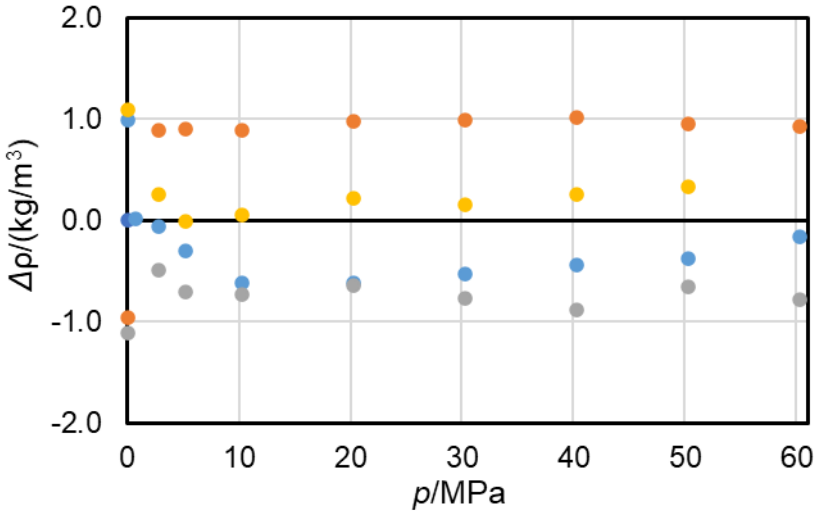

Figure 2. Deviations of the measured water densities and the standard results from NIST REFPROP (●, 298.15 K; ●, 343.15 K; ●, 398.15 K; ●, 448.15 K).

Prior to use, the VTD was flushed with isopropanol and dried under vacuum. Crude oil was drawn into the evacuated apparatus from a glass storage bottle fitted with a dip tube connected to the inlet of the syringe pump. The system pressure and temperature were raised by the syringe pump and the oven, respectively. The target temperatures were 298.15, 343.15, 393.15 K and 448.15 K. On each isotherm, density measurements started at a pressure of 1 MPa, continued at 5 MPa and then proceeded from 10 MPa to 60 MPa in steps of 10 MPa. Finally, the pressure was returned to 1 MPa to check the repeatability. In the case of measurements on pure substances and homogeneous mixtures, the standard uncertainty of density obtained with this apparatus is of the order of 1 kg·m^{-3}. However, crude oils are complex fluids and composition changes can occur during measurements - for example, because of solids precipitation at high temperatures and pressures. We compared our density values extrapolated to p = 0.1 MPa with measurements made in Shell's laboratory using a similar vibrating-tube densimeter but limited to atmospheric pressure and to temperatures not exceeding 343 K. The present results were found to deviate by between -2 and +5 kg·m^{-3} and, taking these into account, we estimate the overall combined standard uncertainty of our data to be 4 kg·m^{-3}.

The measured densities of each oil were correlated by the modified Tait equation [47],

$$\rho = \rho_0 \left[1 - C \log_{10} \left(\frac{p + B}{p_0 + B} \right) \right]^{-1} \tag{3}$$

where p_0 = 0.1 MPa, C = 0.2, and ρ_0 and B are correlated as follows,

$$\rho_0 \,/\, (\mathrm{kg \cdot m^{-3}}) = \sum_{i=0}^{2} a_i (T \,/\, K)^i \tag{4}$$

$$B \,/\, \mathrm{MPa} = \sum_{i=0}^{2} b_i (T \,/\, K)^i \tag{5}$$

The adjustable parameters in the Tait equation for each crude oil are listed in Table 4. Fig. 3 shows the measured and correlated densities of the three crude oil samples. It is found the Tait equation provided a very precise representation of the experimental data and we therefore ascribe the standard uncertainty of the experimental data, *i.e.* 4 kg·m^{-3}, to the correlation.

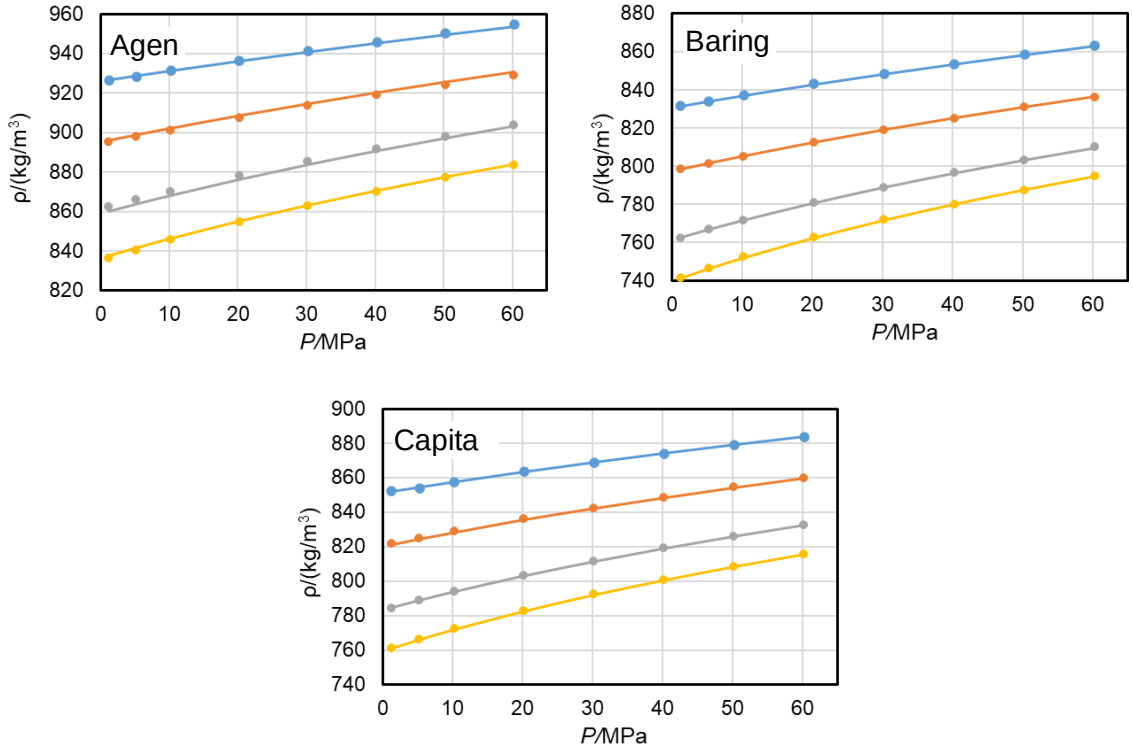

Figure 3. Measured and correlated densities of three oil samples at the pressures up to 60 MPa and the temperatures up to 423.15 K. Symbol are experimental data and curves represent the correlation: ●, 298.15 K; ●, 343.15 K; ●, 393.15 K; ●, 423.15 K.

The oil and aqueous phases were treated as immiscible for the purposes of estimating the density difference $\Delta\rho$. This assumption is consistent with the very low mutual solubility of

hydrocarbons and water at the temperatures investigated. Although we observe dynamic effects in the IFT these are attributed to diffusion and adsorption of surface-active components present at very low concentration such that migration has a negligible influence on the density.

Table 4. Parameters in Equations 3 to 5 for density.

Oil	a_0	a_1	a_2	b_0	b_1	b_2
Agen	1090.60	-0.4242	$-4.186 \cdot 10^{-3}$	850.95	-3.5019	$3.918 \cdot 10^{-3}$
Baring	1075.88	-0.8760	$1.922 \cdot 10^{-3}$	442.40	-1.5294	$1.419 \cdot 10^{-3}$
Capita	979.00	-0.2066	$-7.386 \cdot 10^{-3}$	393.25	-1.2399	$1.011 \cdot 10^{-3}$

Results and discussion

Measured interfacial tension

As a validation, the IFT of the *n*-decane–water system was measured at T = 298.15 K and P = 0.1 MPa and found to be 51.9 $mN \cdot m^{-1}$. This value is in good agreement with available literature results of 50.5 $mN \cdot m^{-1}$ [24], 51.2 $mN \cdot m^{-1}$ [48], 51.98 $mN \cdot m^{-1}$ [28] at the same temperature and pressure conditions. A total of 27 series of IFT measurements were conducted for combinations of the three crude oils with pure water and the two synthetic reservoir brines at the temperatures of 298.15, 343.15, 393.15 K and pressures up to 30 MPa. The full dynamic results are shown graphically in Figs. S2–S4 of the Supplementary Materials. Representative cases are selected and plotted in Figs. 4-7 to represent the dynamic evolution of interfacial tensions between the three crude oils and aqueous phases at different conditions. In general, one can observe in the figures that the dynamic IFT vs. time curve is divided into two major regimes. More specifically, most oil-water and oil-brine dynamic IFTs at both low and high temperatures/pressures are rapidly reduced within a short initial time, followed by a long period with relatively small IFT variations. Obviously, the IFTs at the early stage of interface formation (i.e., at 1 s) are higher than the IFTs at any later time. This is because the oil-water/brine interface, and newly formed drop volume are prime initially, tending to equilibrate as a result of diffusing species. Furthermore, and in contrast to some previous studies [49,50], no induction period was observed in the current measurements. Considering there was maximum 2 s time difference between drop formation and measurements starting one can conclude that the induction period, if any, is shorter than 2 s under the conditions investigated.

Fig. 4 shows the measured dynamic interfacial tensions of Agen against water and brines at the three temperatures and at pressures of 0.5, 5 and 30 MPa. Most cases follow a typical

evolution pattern in which the IFT reduces rapidly within a short initial period of order 10^2 s and then gradually approaches a long-term equilibrium value. However, in some atypical cases, the IFT passes through a minimum value after initial reduction and gradually rises to a long-term equilibrium value which is nevertheless below the initial IFT. This behavior is exemplified here by the Agen oil–water system at T = 393.15 K and pressures of 0.5 and 5 MPa. Generally, the observed behavior in both typical and atypical cases was found to be repeatable as evidenced by the three repeated measurements performed at each state point. At the lowest temperature investigated, it was generally found that the oil-brine IFT was slightly lower than the oil-water IFT at the same pressure; however, at high temperatures the oil-water and oil-brine IFTs were similar. Furthermore, the oil-brine IFTs were found to be very similar for the sandstone and carbonate brines under the same temperature and pressure conditions, indicating the brine chemistry had a minimal effect. Moreover, it is seen from the three figures that the Agen oil–water IFTs are reduced with increasing temperature, while the oil-brine IFTs don't follow a particular dependence upon temperature. Contrary to the temperature effect, the Agen–water IFTs increase with increasing pressure. The dynamic IFTs of crude oils Baring and Capita against the water and brines at similar conditions are shown in Figs. 5 and 6. The Baring-water, Capita-water and Capita-brine IFTs follow similar patterns to the Agen cases in terms of the dynamic evolution as well as the temperature and pressure influences. However, there are two significant differences between the oils: 1) for Baring and Capita the oil-brine IFTs are always lower than the oil-water IFTs at the same conditions while this is not the case for Agen; 2) most of the atypical dynamic evolutions occur in the Baring case with none observed for Capita. Since the effect of oil compositions on the dynamic IFT evolutions is noticeable, in Fig. 7, the measured IFTs of the three crude oils at a constant pressure of 5 MPa and two temperatures (i.e., 298.15 and 393.15 K) against the respectively water, sandstone and carbonate brines are plotted to clearly present the oil composition effect. Table 5 summaries the rank order of equilibrium IFTs from Figs. 7a–c. Overall, the oil compositions are found to affect the dynamic IFT evolutions and magnitudes to different extents without following any clear pattern. On the other hand, Fig. 7 shows that, in most cases, carbonate-brine exhibits a lower IFT against oil than does the sandstone brine, and this is in accordance with previous studies that identified divalent cations having a larger potential to reduce IFT than mono-valent cations [34].

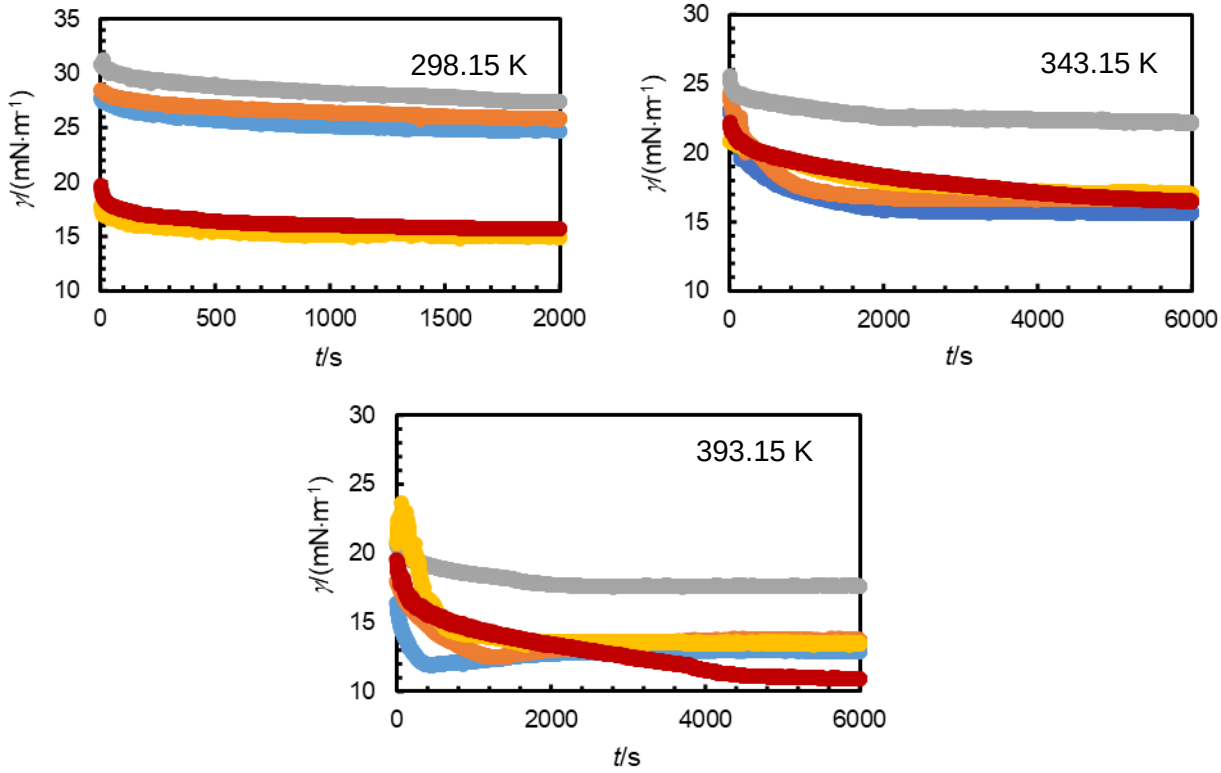

Figure 4. Measured interfacial tensions of crude oil Agen against water and brines at the pressures up to 30 MPa and the temperatures of (a) 298.15 K; (b) 343.15 K; (c) 393.15 K (●, water at 0.5 MPa; ●, water at 5 MPa; ●, water at 30 MPa; ●, sandstone brine at 5 MPa; ●, carbonate brine at 5 MPa): (a) T = 298.15 K; (b) T = 343.15 K; (c) T = 393.15 K.

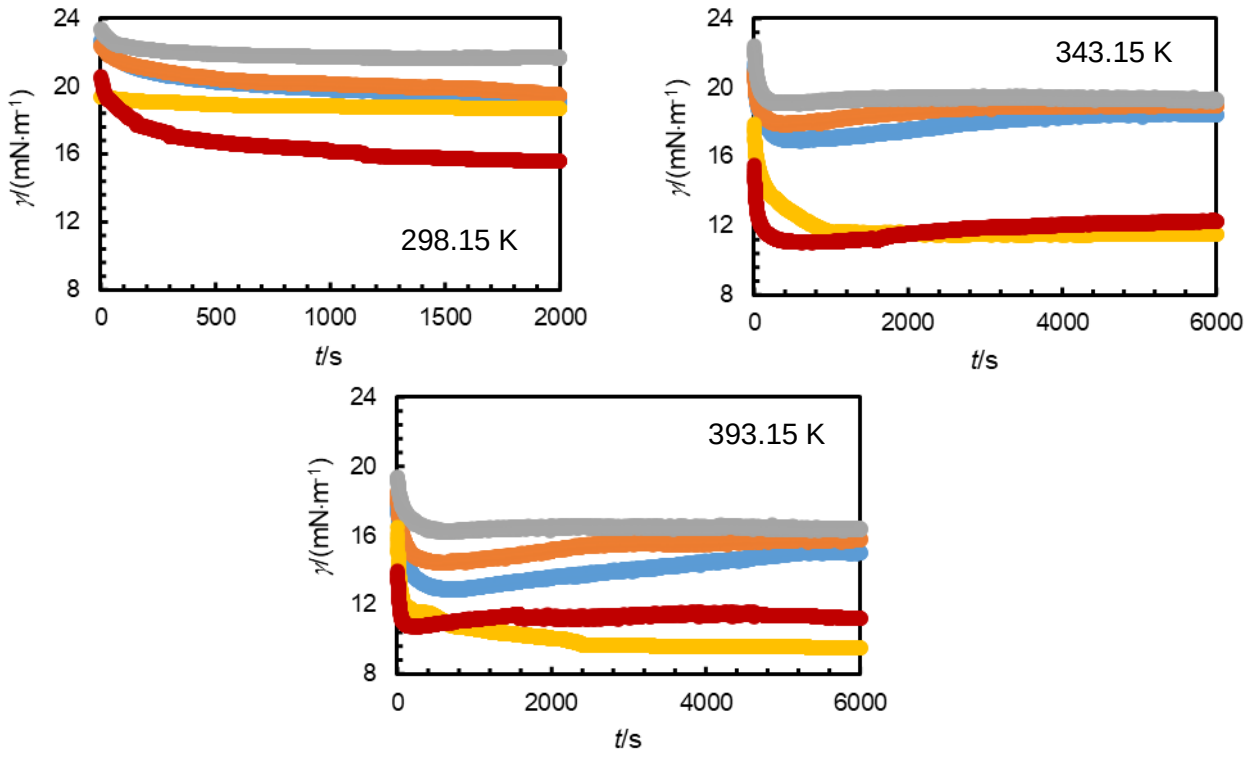

Figure 5. Measured interfacial tensions of crude oil Baring against water and brines at the pressures up to 30 MPa and the temperatures of (a) 298.15 K; (b) 343.15 K; (c) 393.15 K (●, water at 0.5 MPa; ●, water at 5 MPa; ●, water at 30 MPa; ●, sandstone brine at 5 MPa; ●, carbonate brine at 5 MPa): (a) T = 298.15 K; (b) T = 343.15 K; (c) T = 393.15 K.

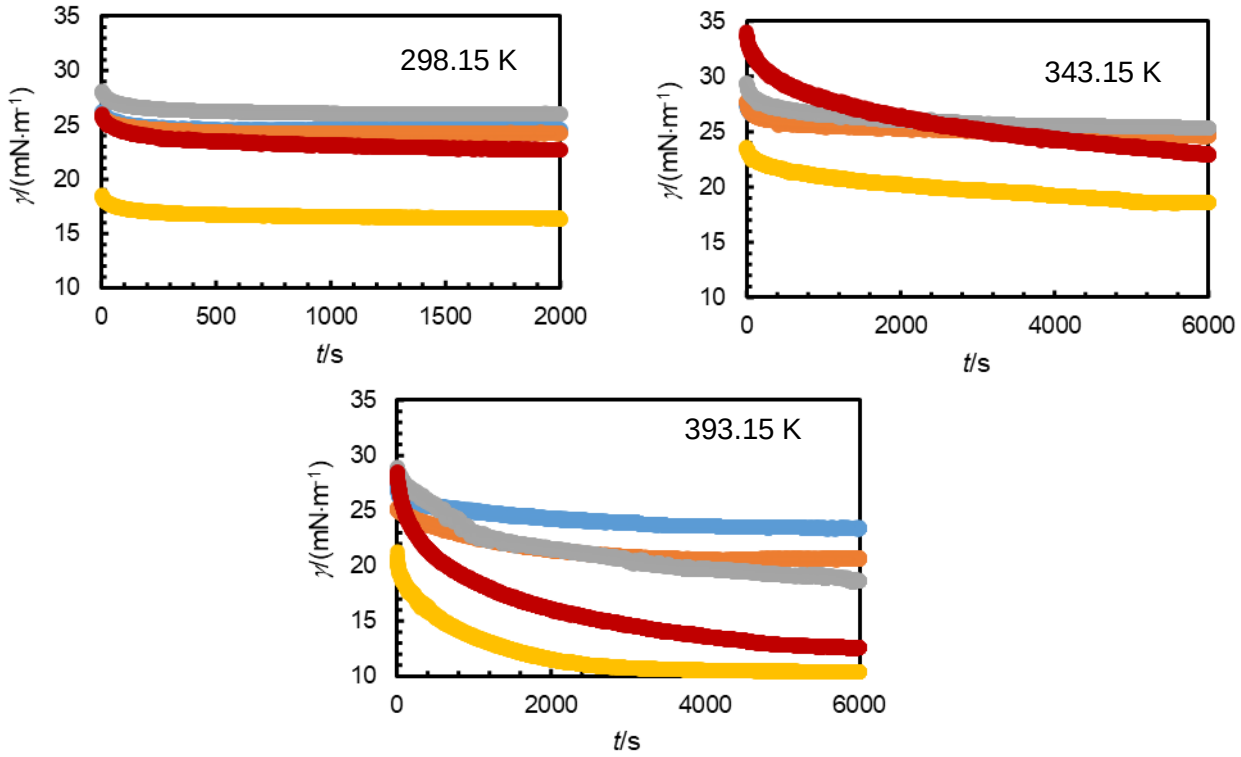

Figure 6. Measured interfacial tensions of crude oil Capita against water and brines at the pressures up to 30 MPa and the temperatures of (a) 298.15 K; (b) 343.15 K; (c) 393.15 K (●, water at 0.5 MPa; ●, water at 5 MPa; ●, water at 30 MPa; ●, sandstone brine at 5 MPa; ●, carbonate brine at 5 MPa): (a) T = 298.15 K; (b) T = 343.15 K; (c) T = 393.15 K.

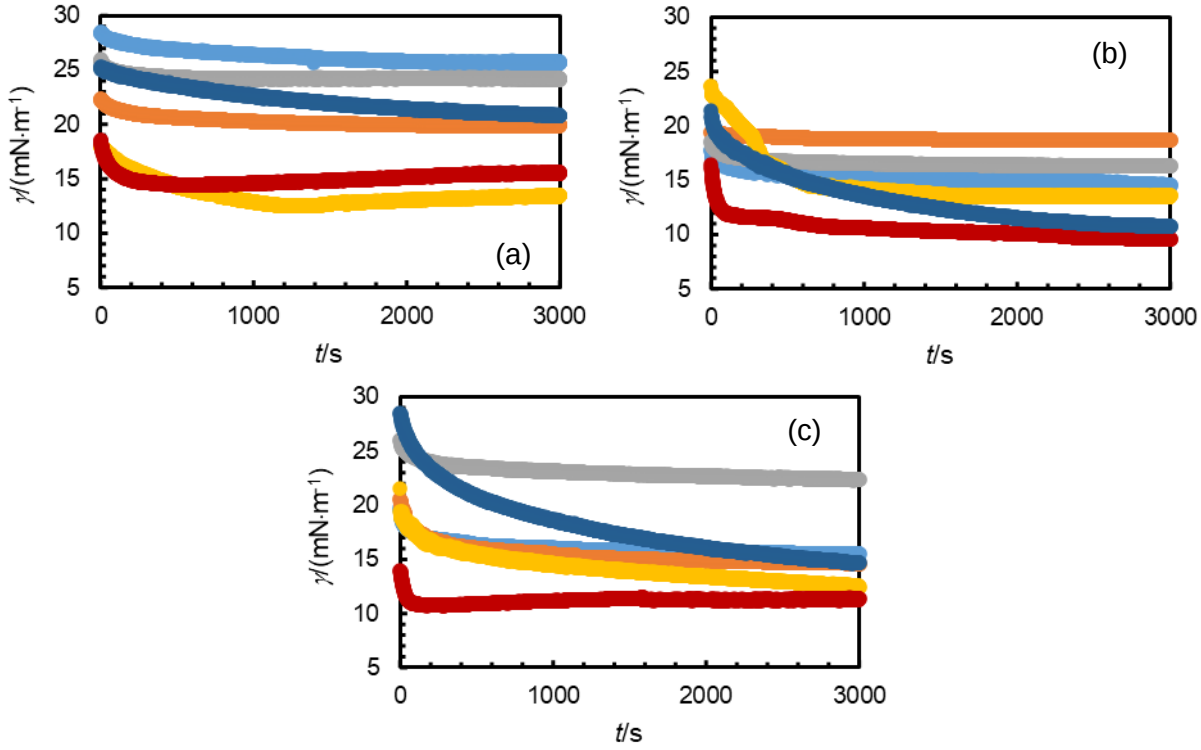

Figure 7. Measured interfacial tensions of crude oils Agen, Baring, and Capita at constant pressure and the temperatures of 298.15 and 393.15 K against (a) water; (b) sandstone brine; (c) carbonate brine (●, Agen at 298.15 K; ●, Baring at 298.15 K; ●, Capita at 298.15; ●, Agen at 393.15 K; ●, Baring at 393.15 K; ●, Capita at 393.15 K): (a) water; (b) sandstone brine; (c) carbonate brine.

Table 5. Rank order of the interfacial tensions at equilibrium in Figure 7.

Aqueous / Temperature	Water	Sandstone brine	Carbonate brine
Low	A > C > B	B > C > A	C > A > B
High	C > A ≈ B	A > C > B	C > A > B

Besides the effects of oil and aqueous compositions, the temperature and pressure effects on the dynamic IFTs are also critically important. Full data presentations which cover the IFTs of the three crude oils against the water and brines over temperature and pressure ranges are shown in Figs. S5–S7 of the supplementary materials at three dynamic stages (i.e., first contact, at 1000 s and at equilibrium). Typically, the IFTs were found to decrease with increasing temperature at all stages of the dynamic evolution, while the effect of pressure is not consistent. Figs. 8–10 shows the equilibrium IFTs of the three crude oils against the water and brines over the relevant temperature and pressure ranges. In comparison with the IFTs observed at 1000 s, the equilibrium Baring-water and Agen- or Capita-water/brine IFTs are almost equivalent to each other, while only the oil Baring-brine IFTs at equilibrium are slightly lower than those at 1000 s, particularly at high temperatures.

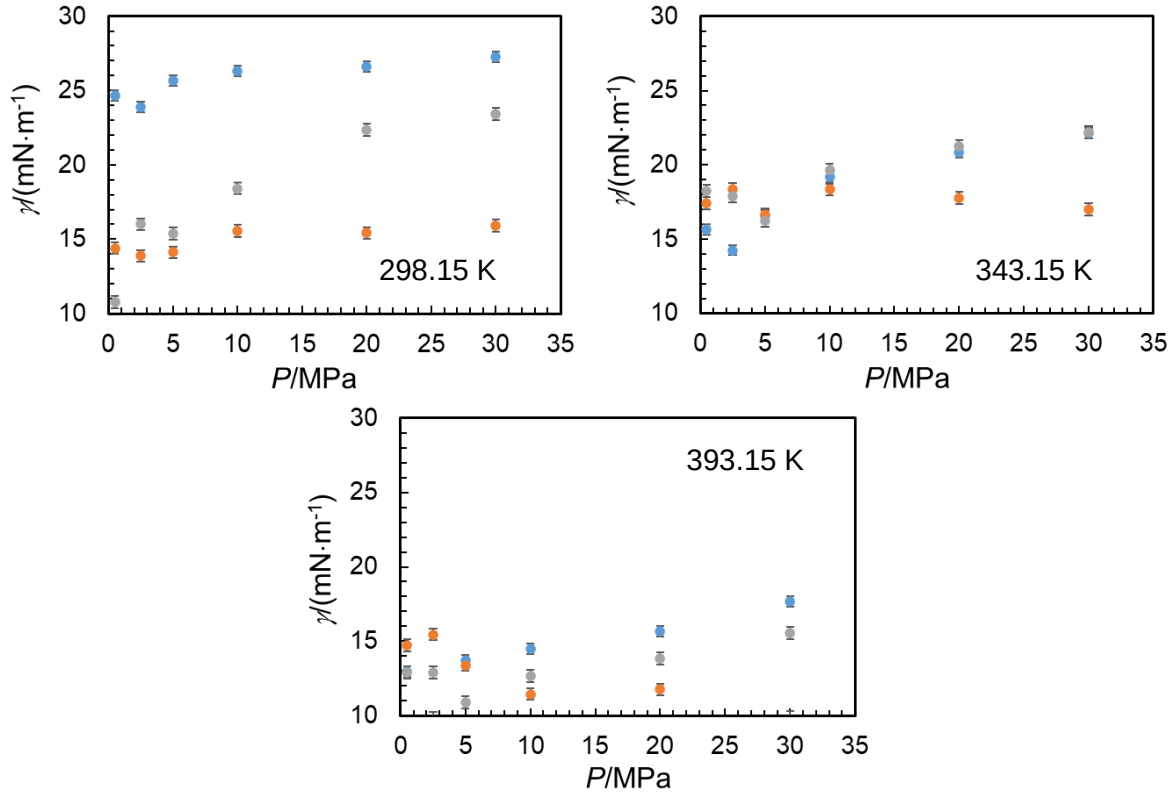

Figure 8. Equilibrium interfacial tensions of crude oil Agen against water and brines at the pressures up to 30 MPa and the temperatures of (a) 298.15 K; (b) 343.15 K; (c) 393.15 K (●, water; ●, sandstone brine; ●, carbonate brine).

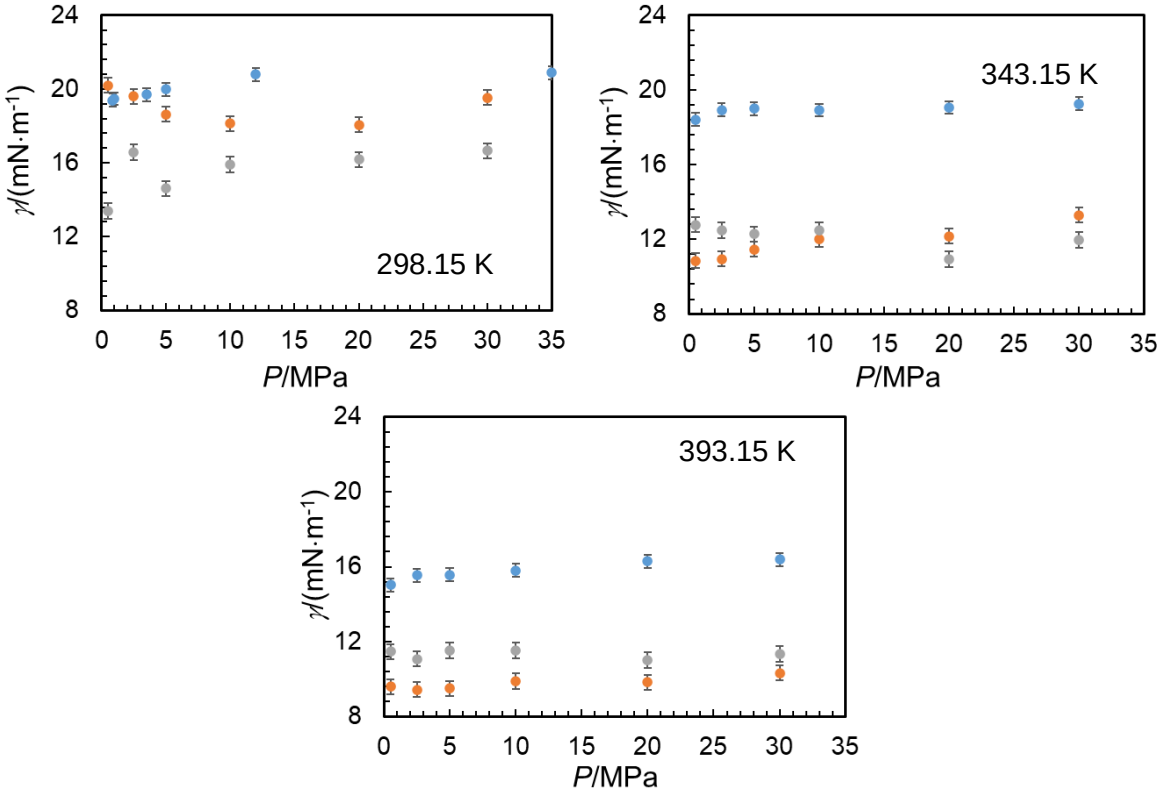

Figure 9. Equilibrium interfacial tensions of crude oil Baring against water and brines at the pressures up to 30 MPa and the temperatures of (a) 298.15 K; (b) 343.15 K; (c) 393.15 K (●, water; ●, sandstone brine; ●, carbonate brine).

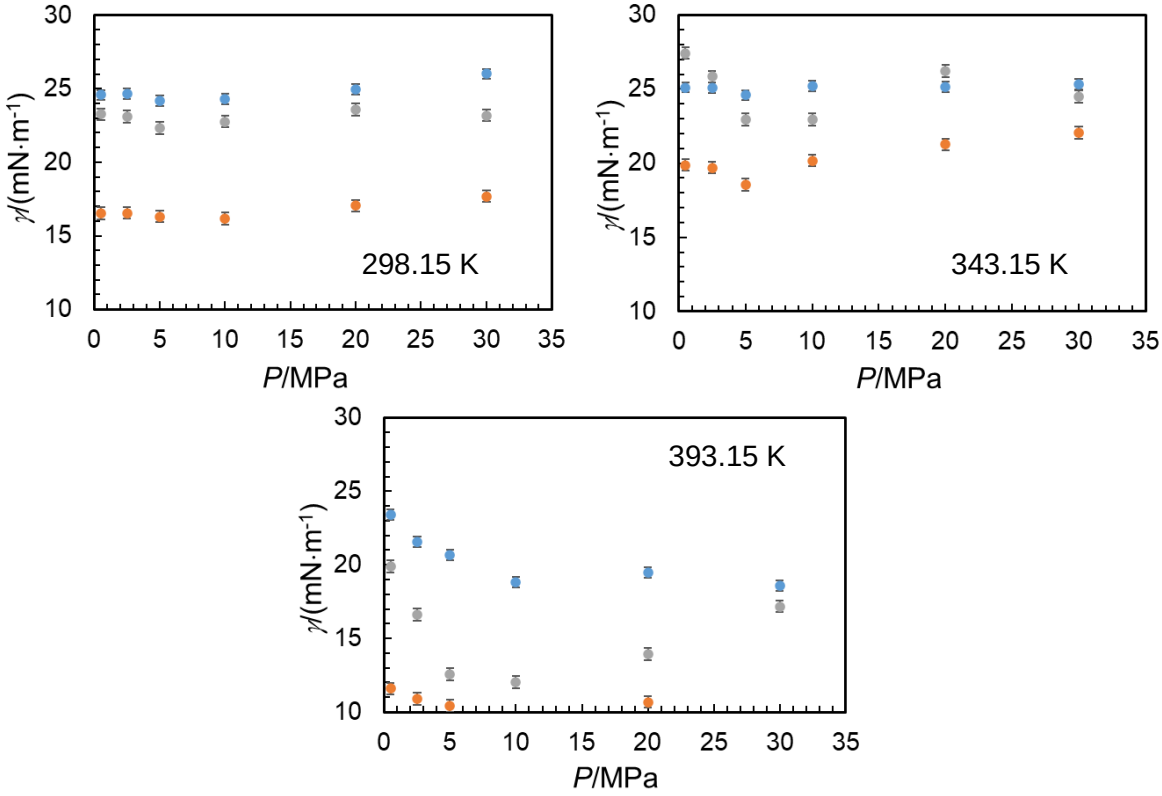

Figure 10. Equilibrium interfacial tensions of crude oil Capita against water and brines at the pressures up to 30 MPa and the temperatures of (a) 298.15 K; (b) 343.15 K; (c) 393.15 K (●, water; ●, sandstone brine; ●, carbonate brine).

Modelling the dynamic interfacial tension

The dynamic crude oil-water and crude oil-brine IFT evolutions vary at different temperature and pressure conditions due to complex fluid compositions involved. As noted, the measured IFTs for all the oil-water and oil-brine systems are rapidly reduced within a short initial time. After that, most typical cases gradually approach a nearly-constant value but several atypical cases are found in which the IFT passes through a minimum before gradually rising towards a steady long-time equilibrium value. These types of dynamic behavior are illustrated schematically in Fig. 11. The physical interpretation of the initial rapid decline of the IFT is based upon diffusion and adsorption. Initially, when the drop is created, the surface-active components are distributed uniformly throughout the oil drop up to the interface. However, SACs have a propensity to adsorb on the surface and hence a process of diffusion to and adsorption on the interface is followed until the interfacial composition is in equilibrium with the bulk-oil composition. This equilibrium can be described by an adsorption isotherm.

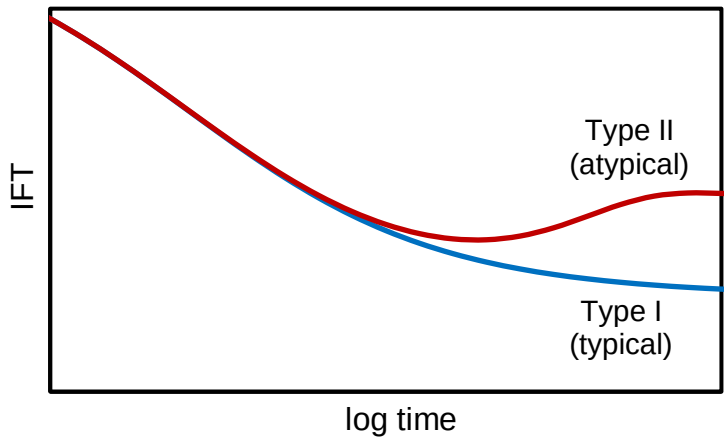

Figure 11. Schematic representation of the typical and atypical time evolutions of the IFT observed in this work.

An analytical model for the diffusion-adsorption process was derived by Sutherland in 1952 [51]. In that model, a plain interface separates semi-infinite slabs or immiscible fluids, one of which (oil in the present case) contains a surface-active solute which can adsorb on the interface but not dissolve into the other phase. Adsorption is assumed to follow a linear isotherm described by Henry's law

$$\Gamma = K_H c, \tag{6}$$

where Γ is surface coverage, K_H is Henry's constant and c is the concentration of surface-active solute in the 'subsurface layer', just below the interface. Under these approximations, the surface coverage Γ at any time t is given by

$$\frac{\Gamma}{\Gamma_\infty} = 1 - \exp\left(\frac{t}{\tau_D}\right)\mathrm{erfc}\left(\sqrt{\frac{t}{\tau_D}}\right) \tag{7}$$

where Γ_∞ is the surface coverage at saturation, $\tau_D = K_H^2/D$ is the diffusion time constant, D is the diffusion coefficient of the SAC and erfc is the complementary error function. The derivation of Eq. (7) is reprised in the Supplementary Material. This model is expected to be reasonably realistic at short times where the surface coverage is small and a linear adsorption isotherm is a reasonable approximation. Since $RT\Gamma = \gamma_0 - \gamma$, where γ_0 is the initial IFT and γ is the IFT at any time, one obtains

$$\gamma = \gamma_0 - (\gamma_0 - \gamma_\infty)\left[1 - \exp\left(\frac{t}{\tau_D}\right)\mathrm{erfc}\left(\sqrt{\frac{t}{\tau_D}}\right)\right], \tag{8}$$

where γ_∞ is the IFT at equilibrium. This function describes a smooth decline of the IFT, initially very rapid, from an initial value of γ_0 towards a final value of γ_∞. The derivation of Sutherland's equation can be found in the supplementary materials.

At short times such that $t/\tau_D << 1$, the exponential and complementary error functions may be expanded in powers of $z = \sqrt{t/\tau_D}$ and, retaining only the leading term, the following short-time approximation is obtained:

$$\gamma \approx \gamma_0 - (\gamma_0 - \gamma_\infty)\sqrt{\frac{t}{\pi\tau_D}} = \gamma_0 - 2RTc_0\sqrt{\frac{Dt}{\pi}}, \tag{9}$$

where c_0 is the concentration of surface-active solute in the bulk of the oil. This approximation gives $\Gamma/\Gamma_\infty = (\gamma_0 - \gamma)/(\gamma_0 - \gamma_\infty)$ to within about 5% for $t/\tau_D \le 0.003$. The second form of Eq. (9) is known as the Ward-Tordai equation [52].

A long-time approximation can also be obtained by noting that, for large z, $\mathrm{erfc}(z) \to \exp(-z^2)/(z\sqrt{\pi})$. In that case,

$$\gamma \to \gamma_\infty + (\gamma_0 - \gamma_\infty)\sqrt{\frac{\tau_D}{\pi t}} = \gamma_\infty + \frac{RT\Gamma_\infty^2}{c_0}\sqrt{\frac{1}{\pi D t}}. \tag{10}$$

This approximation gives $\Gamma/\Gamma_\infty = (\gamma_0 - \gamma)/(\gamma_0 - \gamma_\infty)$ to within about 5% for $t/\tau_D \ge 3$.

Fig. 12 shows the predicted evolution of the reduced surface coverage Γ/Γ_∞ as a function of the dimensionless time t/τ_D according to Sutherland's model, the short-time approximation (Eq. 9) and the long-time approximation (Eq. 10). Of course, Sutherland's model does not reflect the actual geometry of an oil drop surrounded by water or embody a realistic adsorption isotherm. Better-founded theoretical models have been constructed; for example, Fainerman et al. [53] considered a spherical droplet and modelled the diffusion-adsorption process

numerically, while Kairaliyeva et al. adopted a more-realistic Frumkin adsorption isotherm [54]. However, given the complexity of crude oils and the fact that the specific SACs present, their concentrations and adsorption isotherms are typically unknown, the simple Sutherland approximation provides a useful framework within which to rationalize experimental data. Experimental data can be used to estimate the time constant τ_D but it is not possible to determine D or K_H even for a single SAC unless its bulk concentration is also known.

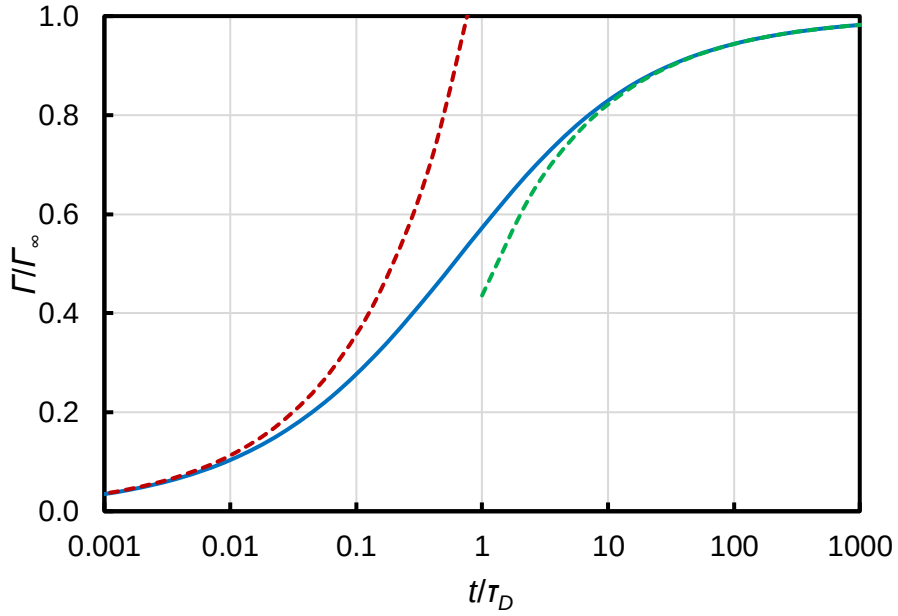

Figure 12. Reduced surface coverage Γ/Γ_∞ as a function of dimensionless time t/τ_D according to Sutherland's model (continuous curve) and the short- and long-time approximations (dashed curves).

In Fig. 13, four examples are presented to show the measured dynamic IFTs of typical and atypical cases in comparison with the Sutherland model with τ, γ_0 and γ_∞ fitted to the experimental data over the first 100 s. It is found that the model matches the dynamic IFTs of both typical and atypical cases up to a time of several hundred seconds. In terms of the long-term dynamic evolution, the current model is inapplicable for either typical or atypical cases, though the deviations for the typical cases are smaller, given that the model is only valid for the diffusion-control period. The typical behavior observed in this work is very similar to that observed in studies of the surface tension of aqueous surfactant solutions [48, 49] where the diffusion-adsorption model is able to provide a quantitative account of the data. The case of crude oils is much more complex with probably many different SACs present. These SACs are mainly found within the asphaltene fraction of crude oils which, when extracted and added to a model oil-water system, give rise to behavior very similar to what we observe at short times [55]. The resins and carboxylic acids present in crude oils also exhibit surface-active behavior [56]. Furthermore, it is expected that the long-term behavior is affected by other

phenomena, for example, molecular rearrangement of SAC on the interface. It should be noted that empirical equations were used in the literature to model long-term IFT evolutions [55,57,58].

The atypical behavior observed in this work is similar to that reported by Verruto et al. [59] who used interfacial tensiometry and both shear and dilatational rheology to study the adsorption and molecular rearrangement of asphaltenic films at the oil-brine interface. They observed the atypical behavior emerging with increasing *p*H of the aqueous phase and connected it with both molecular rearrangement of the SACs on the interface and transfer of a fraction of these SACs to the aqueous phase. Molecular rearrangements of SAC at an oil-water interface have also been observed in other systems. For example, Zhai et al. used spectroscopy and interferometry to characterize the time evolution of the conformation of a surface-active protein, β-lactoglobulin, at oil-water interfaces [60]. They observed complex evolution of the interface thickness, mass and refractive index over time, consistent with conformational changes. We have also considered the possibility that atypical behavior might be associated with SACs dissolving into the aqueous phase on a long time scale. However, analysis of the aqueous phase by UV-Vis spectroscopy did not yield conclusive result.

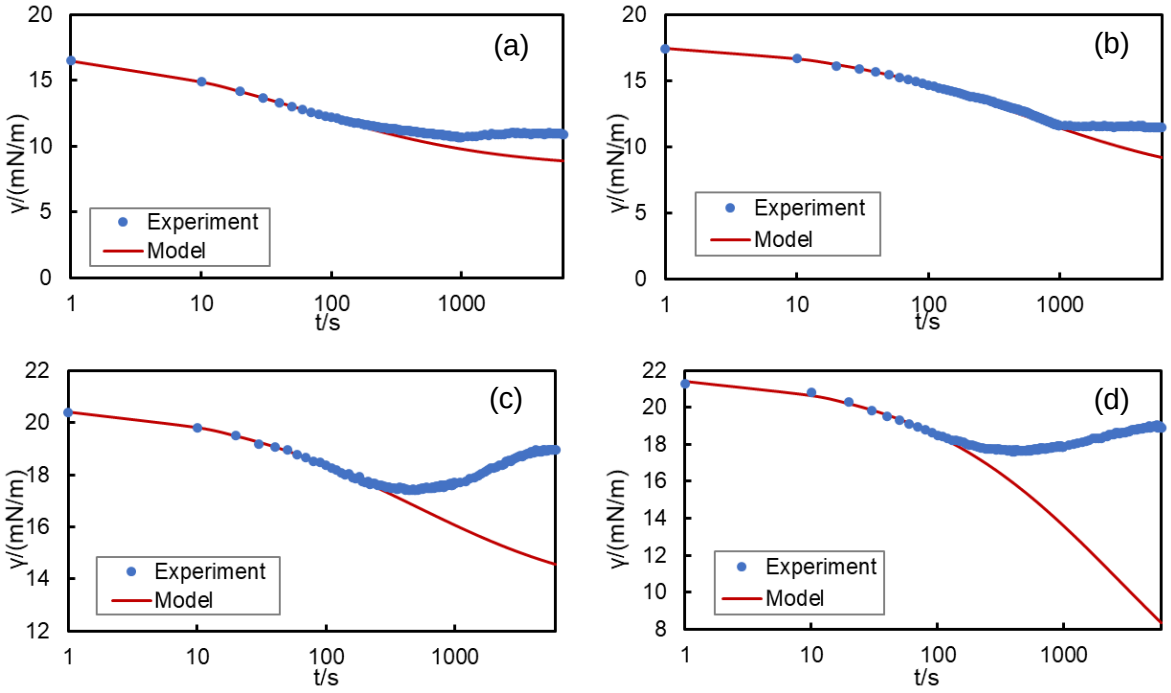

Figure 13. Measured and simulated dynamic interfacial tensions within an initial short-term period: (a) and (b) typical case; (c) and (d) atypical case.

In order to distinguish between the typical and atypical dynamic IFT behavior, we introduce an objective criterion. Specifically, the case is considered to be atypical when the difference of the IFTs at t = 1000 s and at 'equilibrium' is larger than 0.1 mN·m^{-1}. This threshold value

allows for experimental uncertainties and is designed to select as atypical only those states in which there is a significant 'recovery' of the IFT after the period of decline. This analysis showed that, with just two exceptions, all of the atypical cases were observed for the Baring oil. The distribution of typical and atypical cases in temperature-pressure co-ordinates for Baring oil with the different aqueous phases is shown in Fig. 14. Here, the atypical cases are seen to be mainly confined to the two higher temperatures studied and to the cases where the aqueous phase was either water or carbonate brine. The other cases in which atypical behavior was found were for the Agen oil-water system at T = 393.15 K and low pressures.

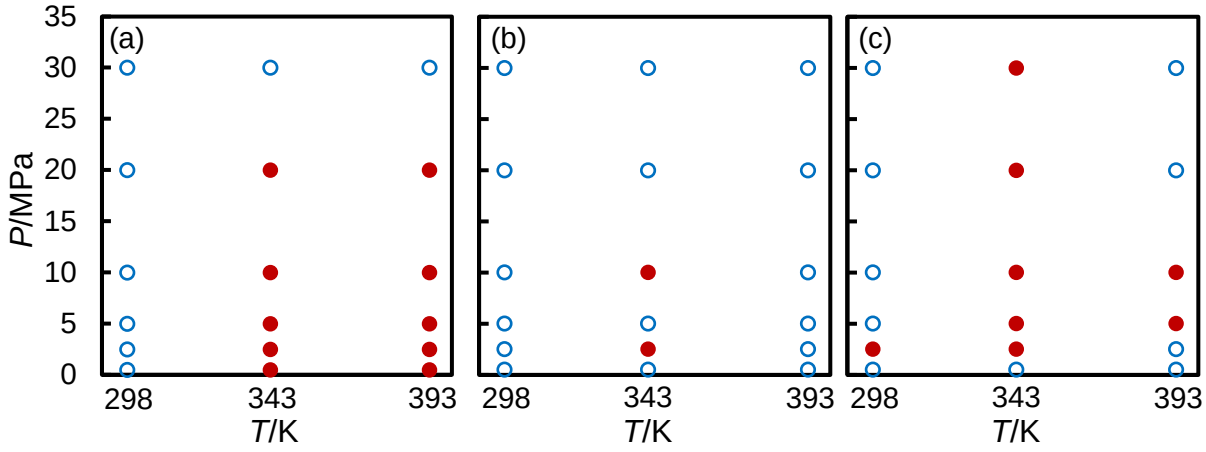

Figure 14. Categorization of the IFT evolutions for Baring oil with different aqueous phases as a function of temperature and pressure: ○, typical case; ●, atypical case. (a) water; (b) sandstone brine; (c) carbonate brine.

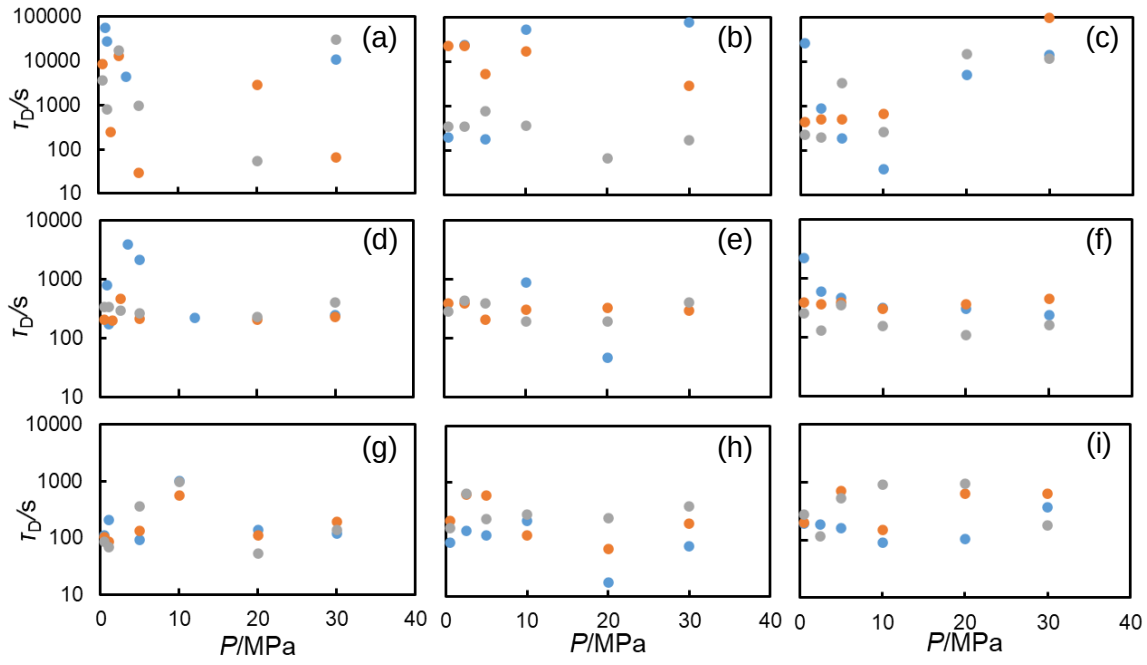

Figure 15. Diffusion time constant (τ_D) at temperatures up to 393.15 K and pressures up to 30 MPa for the systems of: (a) Agen-water; (b) Agen-sandstone brine; (c) Agen-carbonate brine; (d) Baring-water; (e) Baring-sandstone brine; (f) Baring-carbonate brine; (g) Capita-water; (h)

Capita-sandstone brine; (i) Capita-carbonate brine (●, T = 298.15 K; ●, T = 343.15 K; ●, T = 393.15 K).

Finally, in Fig. 15, we plot the characteristic diffusion time constants τ_D against pressure for all investigated systems and conditions. The time constant does not exhibit smooth trends with temperature and/or pressure but once can observe that most fall in the range of 10^2 to 10^3 s, with longer values being observed most frequently for the Agen oil. There is a tendency for the time constant to be greater for oil-brine systems than for the corresponding oil-water system.

Conclusions

In this paper, dynamic interfacial tensions of the three crude oil-water and crude oil-brine systems are reported at temperatures of 298.15, 343.15, 393.15 K and pressures up to 30 MPa. The following six conclusions are supported:

1. The dynamic evolution of the crude oil-water and crude oil-brine IFT is divided into two major regimes: an initial rapid decline followed by a long-term equilibration. No induction period has been observed in this work and so it can be concluded that any such period is of duration < 2 s.
2. As a general trend, the measured IFTs decrease with increasing temperature, while the pressure effect is mild and inconsistent. However, it can be concluded that the effect of pressure on the IFT is relatively greater at higher temperatures which may reflect the increased compressibility of the oil under those conditions.
3. In comparison with the oil-water cases, crude oil-brine IFTs are always lower, and the dynamics are usually slower. Additionally, the calcium-ion containing carbonate-brine systems generally exhibit lower IFTs against the oils than do the sandstone brine systems.
4. Although the crude-oil type gives rise to substantial differences in the IFT, oil composition does not correlate obviously with the observed behavior at equilibrium. From the 2D-GC analysis, Baring and Capita appear quite similar, while Agen is distinguished by a lack of paraffines and a higher aromatic content. However, the rank orders seen in Table 5 do not distinguish the equilibrium IFT for the Agen systems from the others. This suggests that the equilibrium IFT is influenced by minor components, such as polar molecules, that are not specifically identified in the 2D-GC analysis. On the other hand, the dynamics as summarized in Fig. 15 are generally slower for the Agen oil and this may reflect slower diffusion in this much-more viscous oil. Accordingly, one can conclude the any prediction method for equilibrium oil-water IFT based on a composition

analysis, even a sophisticated 2D-GC analysis, might not be reliable owing to the strong influence of some minor components.

5. The dynamic IFT evolution can be represented by Sutherland's model over an initial diffusion-controlled period extending to between 10^2 s and 10^3 s and the characteristic time constants most fall in the range of 10^2 to 10^3 s. The model is not able to represent the long-time behavior for either typical or atypical cases and this is an area for further study.
6. A quantitative criterion can be applied to differentiate the typical and atypical IFT evolution and it was found that the vast majority of the atypical cases occurred with just one of the oils (Baring) and mostly at temperatures of 343.15 K and 393.15 K. Two atypical cases were also observed for Agen oil at the highest experimental temperature only. Again, this behavior does not correlate with the bulk composition but it might reflect the nature of surface-active components present at trace levels.

Acknowledgement

The authors gratefully acknowledge funding from the Shell Digital Rocks Programme at Imperial College London.

References

[1] Chen H, Han L, Luo P, Ye Z. The ultralow interfacial tensions between crude oils and gemini surfactant solutions. J Colloid Interface Sci 2005;285:872–4.

[2] Espinoza DN, Santamarina JC. Water-CO_2-mineral systems: Interfacial tension, contact angle, and diffusion—Implications to CO_2 geological storage. Water Resour Res 2010;46.

[3] Roe R-J. Interfacial tension between polymer liquids. J Colloid Interface Sci 1969;31:228–35.

[4] Zhang K, Jia N, Li S, Liu L. Rapid Determination of Interfacial Tensions in Nanopores: Experimental Nanofluidics and Theoretical Models. Langmuir 2019;35:8943–9.

[5] Girifalco LA, Good RJ. A theory for the estimation of surface and interfacial energies. I. Derivation and application to interfacial tension. J Phys Chem 1957;61:904–9.

[6] Ameli F, Hemmati-Sarapardeh A, Schaffie M, Husein MM, Shamshirband S. Modeling interfacial tension in N_2/*n*-alkane systems using corresponding state theory: Application to gas injection processes. Fuel 2018;222:779–91.

[7] Zhang K, Tian L, Liu L. A new analysis of pressure dependence of the equilibrium interfacial tensions of different light crude oil–CO_2 systems. Int J Heat Mass Transf 2018;121:503–13.

[8] Steegmans MLJ, Warmerdam A, Schroen KGPH, Boom RM. Dynamic interfacial

tension measurements with microfluidic Y-junctions. Langmuir 2009;25:9751–8.
[9] Drelich J, Fang C, White CL. Measurement of interfacial tension in fluid-fluid systems. Encycl Surf Colloid Sci 2002;3:3158–63.
[10] Cayias JL, Schechter RS, Wade WH. The measurement of low interfacial tension via the spinning drop technique, ACS Publications; 1975.
[11] Rao DN. A new technique of vanishing interfacial tension for miscibility determination. Fluid Phase Equilib 1997;139:311–24.
[12] Zhang K, Jia N, Li S. Exploring the effects of four important factors on oil–CO_2 interfacial properties and miscibility in nanopores. RSC Adv 2017;7:54164–77.
[13] Li X-S, Liu J-M, Fu D. Investigation of interfacial tensions for carbon dioxide aqueous solutions by perturbed-chain statistical associating fluid theory combined with density-gradient theory. Ind Eng Chem Res 2008;47:8911–7.
[14] Gloor GJ, Jackson G, Blas FJ, Del Rio EM, De Miguel E. Prediction of the vapor− liquid interfacial tension of nonassociating and associating fluids with the SAFT-VR density functional theory. J Phys Chem C 2007;111:15513–22.
[15] Cheng P, Li D, Boruvka L, Rotenberg Y, Neumann AW. Automation of axisymmetric drop shape analysis for measurements of interfacial tensions and contact angles. Colloids and Surfaces 1990;43:151–67.
[16] Yang D, Tontiwachwuthikul P, Gu Y. Interfacial interactions between reservoir brine and CO_2 at high pressures and elevated temperatures. Energy & Fuels 2005;19:216–23.
[17] Georgiadis A, Maitland G, Trusler JPM, Bismarck A. Interfacial tension measurements of the (H_2O+ CO_2) system at elevated pressures and temperatures. J Chem Eng Data 2010;55:4168–75.
[18] Li X, Boek ES, Maitland GC, Trusler JPM. Interfacial Tension of (Brines+ CO_2): $CaCl_2$ (aq), $MgCl_2$ (aq), and Na_2SO_4 (aq) at Temperatures between (343 and 423) K, Pressures between (2 and 50) MPa, and Molalities of (0.5 to 5) mol· kg^{-1}. J Chem Eng Data 2012;57:1369–75.
[19] Rotenberg Y, Boruvka L, Neumann Aw. Determination of surface tension and contact angle from the shapes of axisymmetric fluid interfaces. J Colloid Interface Sci 1983;93:169–83.
[20] Georgiadis A, Maitland G, Trusler JPM, Bismarck A. Interfacial tension measurements of the (H_2O+ n-decane+ CO_2) ternary system at elevated pressures and temperatures. J Chem Eng Data 2011;56:4900–8.
[21] Zhang K, Gu Y. Two new quantitative technical criteria for determining the minimum miscibility pressures (MMPs) from the vanishing interfacial tension (VIT) technique. Fuel 2016;184:136–44.
[22] Hassan ME, Nielsen RF, Calhoun JC. Effect of pressure and temperature on oil-water interfacial tensions for a series of hydrocarbons. J Pet Technol 1953;5:299–306.

[23] Aveyard R, Haydon DA. Thermodynamic properties of aliphatic hydrocarbon/water interfaces. Trans Faraday Soc 1965;61:2255–61.
[24] Jennings Jr HY. The effect of temperature and pressure on the interfacial tension of benzene-water and normal decane-water. J Colloid Interface Sci 1967;24:323–9.
[25] McCaffery FG. Measurement of interfacial tensions and contact angles at high temperature and pressure. J Can Pet Technol 1972;11.
[26] Matubayasi N, Motomura K, Kaneshina S, Nakamura M, Matuura R. Effect of pressure on interfacial tension between oil and water. Bull Chem Soc Jpn 1977;50:523–4.
[27] Cai B-Y, Yang J-T, Guo T-M. Interfacial tension of hydrocarbon+ water/brine systems under high pressure. J Chem Eng Data 1996;41:493–6.
[28] Zeppieri S, Rodríguez J, López de Ramos AL. Interfacial tension of alkane + water systems. J Chem Eng Data 2001;46:1086–8.
[29] Al-Sahhaf T, Elkamel A, Suttar Ahmed A, Khan AR. The influence of temperature, pressure, salinity, and surfactant concentration on the interfacial tension of the n-octane-water system. Chem Eng Commun 2005;192:667–84.
[30] Firoozabadi A, Ramey Jr HJ. Surface tension of water-hydrocarbon systems at reservoir conditions. J Can Pet Technol 1988;27.
[31] Goebel A, Lunkenheimer K. Interfacial tension of the water/*n*-alkane interface. Langmuir 1997;13:369–72.
[32] Xu W. Experimental investigation of dynamic interfacial interactions at reservoir conditions 2005.
[33] Moeini F, Hemmati-Sarapardeh A, Ghazanfari M-H, Masihi M, Ayatollahi S. Toward mechanistic understanding of heavy crude oil/brine interfacial tension: The roles of salinity, temperature and pressure. Fluid Phase Equilib 2014;375:191–200.
[34] Lashkarbolooki M, Ayatollahi S, Riazi M. The impacts of aqueous ions on interfacial tension and wettability of an asphaltenic–acidic crude oil reservoir during smart water injection. J Chem Eng Data 2014;59:3624–34.
[35] Perles CE, Guersoni VCB, Bannwart AC. Rheological study of crude oil/water interface–The effect of temperature and brine on interfacial film. J Pet Sci Eng 2018;162:835–43.
[36] Rücker M, Bartels W, Singh K, Brussee N, Coorn A, van der Linde HA, et al. The effect of mixed wettability on pore-scale flow regimes based on a flooding experiment in Ketton limestone. Geophys Res Lett 2019;46:3225–34.
[37] Rücker M, Bartels W-B, Garfi G, Shams M, Bultreys T, Boone M, et al. Relationship between wetting and capillary pressure in a crude oil/brine/rock system: From nano-scale to core-scale. J Colloid Interface Sci 2020;562:159–69.
[38] Zheng L, Rücker M, Bultreys T, Georgiadis A, Mooijer-van den Heuvel MM, Bresme F, et al. Surrogate models for studying the wettability of nanoscale natural rough surfaces

using molecular dynamics. Energies 2020;13:2770.

[39] Zheng L. Molecular Modelling and Simulation of Fluids, Surfaces and their Interactions in Reservoir Settings. PhD Thesis Imp Coll London 2020.

[40] Lv P, Stevar MSP, Trusler JPM. Interfacial tensions in the (CH_4 + CO_2 + H_2O) system under two- and three-phase conditions. Fluid Phase Equilib 2020;522:112760.

[41] Pan ziqing, Trusler JPM. Refractive-Index Effects in Pendant Drop Tensiometry. Meas Sci Technol 2021;submitted.

[42] Lemmon EW, Huber ML, McLinden MO. NIST Standard Reference Database 23: Reference Fluid Thermodynamic and Transport Properties-REFPROP, Version 8.0. National Institute of Standards and Technology, Standard Reference Data Program. Stand Ref Data Program, Gaithersbg 2018.

[43] Al Ghafri S, Maitland GC, Trusler JPM. Densities of Aqueous $MgCl_2$(aq), $CaCl_2$(aq), KI(aq), NaCl(aq), KCl(aq), $AlCl_3$(aq), and (0.964 NaCl + 0.136 KCl)(aq) at Temperatures Between (283 and 472) K, Pressures up to 68.5 MPa, and Molalities up to 6 mol·kg^{-1}. J Chem Eng Data 2012;57:1288–304.

[44] Al Ghafri SZ, Maitland GC, Trusler JPM. Densities of $SrCl_2$(aq), Na_2SO_4(aq), $NaHCO_3$(aq), and Two Synthetic Reservoir Brines at Temperatures between (298 and 473) K, Pressures up to 68.5 MPa, and Molalities up to 3 mol·kg^{-1}. J Chem Eng Data 2013;58:402–12.

[45] May EF, Tay WJ, Nania M, Aleji A, Al-Ghafri S, Martin Trusler JP. Physical apparatus parameters and model for vibrating tube densimeters at pressures to 140 MPa and temperatures to 473 K. Rev Sci Instrum 2014;85:95111.

[46] Wagner W, Pruß A. The IAPWS formulation 1995 for the thermodynamic properties of ordinary water substance for general and scientific use. J Phys Chem Ref Data 2002;31:387–535.

[47] Caudwell DR, Trusler JPM, Vesovic V, Wakeham WA. Viscosity and density of five hydrocarbon liquids at pressures up to 200 MPa and temperatures up to 473 K. J Chem Eng Data 2009;54:359–66.

[48] Donahue DJ, Bartell FE. The Boundary Tension at Water-Organic Liquid Interfaces. J Phys Chem 1952;56:480–4.

[49] Xu W, Ayirala SC, Rao DN. Measurement of surfactant-induced interfacial interactions at reservoir conditions. SPE Reserv Eval Eng 2008;11:83–94.

[50] Hua XY, Rosen MJ. Dynamic surface tension of aqueous surfactant solutions: I. Basic paremeters. J Colloid Interface Sci 1988;124:652–9.

[51] Sutherland KL. The kinetics of adsorption at liquid surfaces. Aust J Chem 1952;5:683–96.

[52] Ward AFH, Tordai L. Time-dependence of boundary tensions of solutions I. The role of diffusion in time-effects. J Chem Phys 1946;14:453–61.

[53] Teipel U, Aksel N. Adsorption Behavior of Nonionic Surfactants Studied by Drop Volume Technique. Chem Eng Technol 2001;24:393–400.
[54] Kairaliyeva T, Mucic N, Spasojevic L, Bucko S, Katona J, Aksenenko E, et al. Surface Tension Measurements with the Drop Profile Analysis Tensiometry—Consideration of the Surfactant Mass Balance in a Single Drop. Colloids and Interfaces 2017;1.
[55] Rane JP, Harbottle D, Pauchard V, Couzis A, Banerjee S. Adsorption kinetics of asphaltenes at the oil–water interface and nanoaggregation in the bulk. Langmuir 2012;28:9986–95.
[56] Sun T, Zhang L, Wang Y, Peng B, Zhao S, Li M, et al. Dynamic Dilational Properties of Oil–Water Interfacial Films Containing Surface Active Fractions from Crude Oil. J Dispers Sci Technol 2003;24:699–707.
[57] Zhang S, Zhang L, Lu X, Shi C, Tang T, Wang X, et al. Adsorption kinetics of asphaltenes at oil/water interface: Effects of concentration and temperature. Fuel 2018;212:387–94.
[58] Chang C-H, Franses EI. Adsorption dynamics of surfactants at the air/water interface: a critical review of mathematical models, data, and mechanisms. Colloids Surfaces A Physicochem Eng Asp 1995;100:1–45.
[59] Verruto VJ, Le RK, Kilpatrick PK. Adsorption and Molecular Rearrangement of Amphoteric Species at Oil−Water Interfaces. J Phys Chem B 2009;113:13788–99.
[60] Zhai J, Wooster TJ, Hoffmann S V, Lee T-H, Augustin MA, Aguilar M-I. Structural Rearrangement of β-Lactoglobulin at Different Oil–Water Interfaces and Its Effect on Emulsion Stability. Langmuir 2011;27:9227–36.

Measurements and Interpretation of Crude Oil-Water/Brine Dynamic Interfacial Tension at Subsurface Representative Conditions

Kaiqiang Zhang[1], Apostolos Georgiadis[2], J. P. Martin Trusler[1]*

[1]Department of Chemical Engineering, Imperial College London, South Kensington Campus, London SW7 2AZ, United Kingdom

[2]Shell Global Solutions International B.V., 1031 HW Amsterdam, The Netherlands

*Corresponding author: m.trusler@imperial.ac.uk (J. P. M. Trusler)

Supplementary Material

1. Derivation of Sutherland's Formula

In the model, the oil-aqueous phase interface was simplified and assumed to be planar and perpendicular to the x axis, where the oil filled the semi-infinite half space $x \geq 0$ and the aqueous phase filled $x < 0$. The initial condition is the concentration at interface is zero initially, $c = 0$ ($x = 0$, $t = 0$), where c is the concentration, t is time, x is the distance ($x = 0$ at the interface). The analytical solution for diffusion-controlled adsorption model within initial short period (i.e., first 100 s in this study) are derived with Henry's isotherm. First, the Fick's second law is employed to describe the diffuse of surface-active component to interface [1],

$$\frac{\partial c}{\partial t} = D\frac{\partial^2 c}{\partial x^2} \tag{S1}$$

where D is diffusion coefficient. Equation S1 is rearranged as follows by using the fractional calculus,

$$\frac{\partial c}{\partial t} - D\frac{\partial^2 c}{\partial x^2} = (\frac{\partial^{1/2} c}{\partial t^{1/2}} - \sqrt{D}\frac{\partial c}{\partial x})(\frac{\partial^{1/2} c}{\partial t^{1/2}} + \sqrt{D}\frac{\partial c}{\partial x}) = 0 \tag{S2}$$

where $\frac{\partial^{1/2} c}{\partial t^{1/2}}$ is a fractional-time derivative of Riemann–Liouville derivative of order ½, which is defined as,

$$\frac{\partial^{1/2} c}{\partial t^{1/2}} = D_t^{1/2} c(t) = \frac{1}{\Gamma(1/2)}\frac{d}{dt}\int_0^t \frac{c(\tau)}{\sqrt{t-\tau}} d\tau \tag{S3}$$

where $\Gamma(1/2) = \sqrt{\pi}$. In equation S2, the second term is physically meaningful at $x = 0$ so the diffusion in bulk fluid could be described as $\frac{\partial^{1/2} c}{\partial t^{1/2}} = -\sqrt{D}\frac{\partial c}{\partial x}$, which could be expressed by taking $c(x \to 0) = c_0$,

$$\frac{\partial^{1/2} c_0}{\partial t^{1/2}} = -\sqrt{D}(\frac{\partial c_0}{\partial x})_{x=0} \tag{S4}$$

Considering the Fick's first law and its relationship with adsorption,

$$(\frac{\partial c}{\partial t})_{x=0} = D(\frac{\partial c}{\partial x})_{x=0} \Rightarrow \frac{\partial \Gamma_s}{\partial t} = D(\frac{\partial c}{\partial x})_{x=0} \tag{S5}$$

where $\Gamma_s(t) = K_H c(0,t)$. Therefore, two equations which describe the accumulation of surface-active component at interface could be concluded as,

$$\begin{cases} \dfrac{\partial^{1/2} c_0}{\partial t^{1/2}} = -\sqrt{D}(\dfrac{\partial c_0}{\partial x})_{x=0} \\ \dfrac{\partial \Gamma_s}{\partial t} = D(\dfrac{\partial c}{\partial x})_{x=0} \end{cases} \tag{S6a, b}$$

From equations. S5 and S6,

$$D(\frac{\partial c}{\partial x})_{x=0} = \frac{\partial \Gamma_s}{\partial t} = -\sqrt{D}\frac{\partial^{1/2} c_0}{\partial t^{1/2}} \quad \text{(S7)}$$

Equation S7 is rearranged to the following equation by integrating its right-hand side (RHS) through the Riemann–Liouville fractional derivative,

$$\frac{\partial \Gamma_s}{\partial t} = -\frac{\sqrt{D}}{\sqrt{\pi}}[\frac{d}{dt}\int_0^t \frac{c_0(\tau)}{\sqrt{t-\tau}} - \frac{c_0}{\sqrt{\pi t}}] \quad \text{(S8)}$$

The lower limit in the convolution integral in ${}_{RL}D_t^{1/2}$ is zero and the initial condition is $c(0,t) = c_0(t=0) = c_0$ (i.e., a uniform component profile). By applying the operator $D_t^{-1} = \int_0^t dt$ on both sides of equation S8,

$$\Gamma_s(t) = \frac{2c_0\sqrt{D}}{\sqrt{\pi}}\sqrt{t} - \sqrt{D}\frac{1}{\sqrt{\pi}}\int_0^t \frac{c_0(\tau)}{\sqrt{t-\tau}} \quad \text{(S9)}$$

By taking the adsorption isotherm ($c_0(t) = f[\Gamma_s(t)]$) into account, equation S9 could be re-written,

$$\Gamma_s(t) = \frac{2c_0\sqrt{D}}{\sqrt{\pi}}\sqrt{t} - \sqrt{D}\,{}_{RL}D_t^{-1/2}c_0 \quad \text{(S10)}$$

$${}_0D_t^{1/2}(1/\sqrt{t}) = 0,\ {}_0D_t^{1/2}(\sqrt{t}) = \sqrt{\pi}/2$$

Both side of equation S9 is divided by Γ_∞ (saturated surface excess) and also applied with the operator $D_t^{1/2}$,

$$\frac{\partial^{1/2}}{\partial t^{1/2}}(\frac{\Gamma_s(t)}{\Gamma_\infty}) = (\frac{c_0}{\Gamma_\infty})\sqrt{D} - \sqrt{D}(\frac{c_0(t)}{\Gamma_t})(\frac{\Gamma_t}{\Gamma_\infty}) \quad \text{(S11)}$$

Considering $\theta = \Gamma/\Gamma_\infty$, equation S11 is rewritten as,

$$\frac{\partial^{1/2}}{\partial t^{1/2}}\theta + \sqrt{D}(\frac{c_0(t)}{\Gamma_t})\theta = (\frac{c_0}{\Gamma_\infty})\sqrt{D} \quad \text{(S12)}$$

Assume the adsorption isotherm is in the simplest case with the Henry isotherm ($\Gamma = K_H c$), equation S12 is rewritten as,

$$\frac{\partial^{1/2}}{\partial t^{1/2}}\theta + (\frac{\sqrt{D}}{K_H})\theta = (\frac{\Gamma_0}{\Gamma_\infty}K_H)\sqrt{D} \quad \text{(S13)}$$

where $\theta(x=0,t=0) = \theta_0 = \Gamma_0/\Gamma_\infty$. In this case, the semi-derivative of surface excess is ${}_0D_t^{1/2} - \theta_0/\sqrt{\pi t}$ equation S13 could be,

$$\frac{\partial^{1/2}}{\partial t^{1/2}}\theta + (\frac{\sqrt{D}}{K_H})\theta = (\frac{\Gamma_0}{\Gamma_\infty}K_H)\sqrt{D} + \frac{\theta_0}{\sqrt{\pi t}} \quad \text{(S14)}$$

Applying Laplace transform to equation S14,

$$\Theta(p) = \frac{1}{(\sqrt{p} + \sqrt{D}/K_H)}[(\frac{\Gamma_0}{\Gamma_\infty}K_H)\frac{\sqrt{D}}{p} + \frac{\theta_0}{\sqrt{p}}] \quad \text{(S15)}$$

The inverse Laplace transform of equation S15 is,

$$\theta(t) = (\frac{\Gamma_0}{\Gamma_\infty})[1 - \exp(\frac{D}{K_H^2}t)erfc(\frac{\sqrt{D}}{K_H}\sqrt{t})] + \theta_0\exp(\frac{D}{K_H^2}t)erfc(\frac{\sqrt{D}}{K_H}\sqrt{t}) \quad \text{(S16)}$$

If the initial interface is clean ($\theta_0 = 0$), equation S16 could be rearranged as follows with the second term of its RHS is zero within initial very short period,

$$\frac{\Gamma(t)}{\Gamma_\infty} = 1 - \exp(\frac{t}{\tau_D})erfc(\sqrt{\frac{t}{\tau_D}}) \quad \text{(S17)}$$

where τ_D is the dimensionless time, $\tau_D = K_H^2/D$. Equation S17 is exactly the Sutherland's solution (1952) [2].

By using the Taylor expansion of the error function that $\mathrm{erf}(z)=\frac{2}{\sqrt{\pi}}\sum_{n=0}^{\infty}\frac{(-1)^n z^{2n+1}}{n!(2n+1)}=\frac{2}{\sqrt{\pi}}(z-\frac{z^3}{3}+\frac{z^5}{10}-\frac{z^7}{42}+\frac{z^9}{216}-...)$, the approximate solution of error function in equation S16 could be expressed as follows,

$$erfc\left(\sqrt{Dt}\,/\,K_H\right)=\frac{2}{\sqrt{\pi}}\cdot\frac{\sqrt{Dt}}{K_H} \tag{S18}$$

Given that $\Gamma_0=K_H C_0$ (Henry's law), equation S17 could be rearranged as,

$$\Gamma_t=K_H C_0\cdot\exp\left(\frac{Dt}{K_H^2}\right)\cdot\frac{2}{\sqrt{\pi}}\cdot\frac{\sqrt{Dt}}{K_H}=2\sqrt{\frac{Dt}{\pi}}C_0\cdot\exp\left(\frac{Dt}{K_H^2}\right) \tag{S19}$$

By assuming $\exp\left(\frac{Dt}{K_H^2}\right)$ to be unity (Dt is much smaller than K_H^2 so $\frac{Dt}{K_H^2}$ is very close to zero), equation S19 could be simplified as,

$$\Gamma_t=2\sqrt{\frac{Dt}{\pi}}C_0 \tag{S20}$$

Since $\Gamma_t=\frac{\gamma_0-\gamma_t}{RT}$, equation S20 is rewritten as,

$$\gamma_t=\gamma_0-2RTC_0\sqrt{\frac{D}{\pi}}\sqrt{t} \tag{S21}$$

The above equation is an empirically approximate solution of equation S17, which indicates that γ_t is quadratically correlated with $\sqrt{t}$ within the short-term diffusion-control period.

2. Supplementary figures

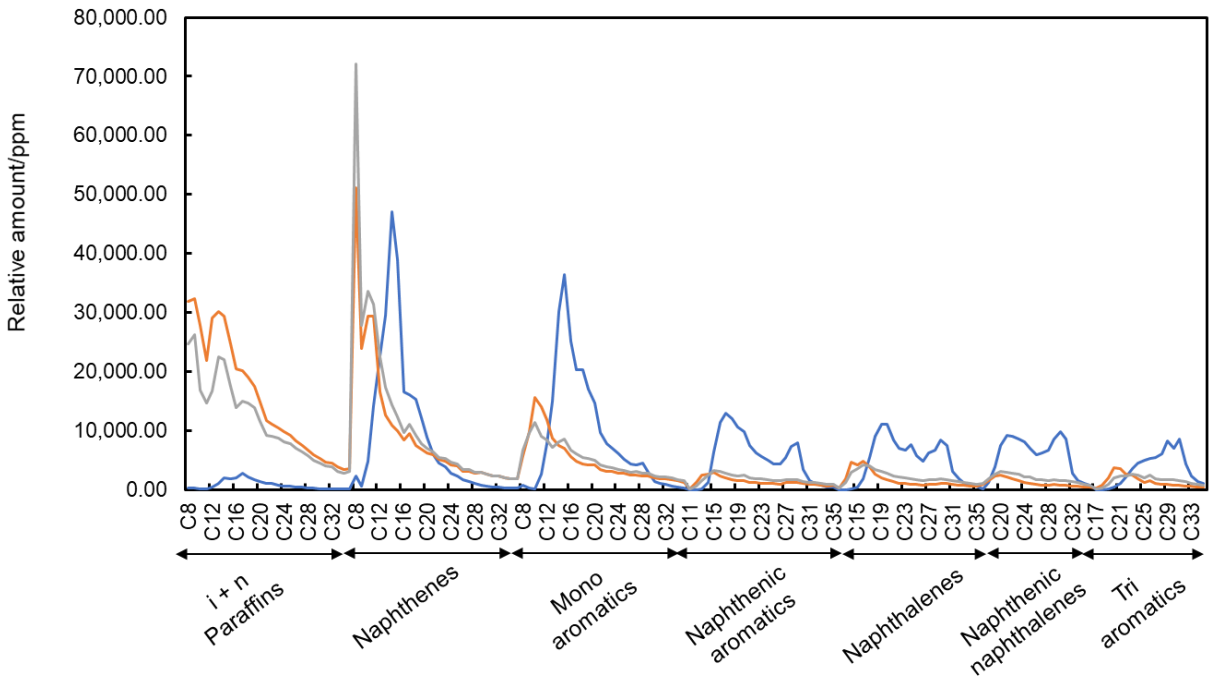

Figure S1 Two-dimensional gas chromatography results of Agen (—), Baring (—), and Capita (—) oils.

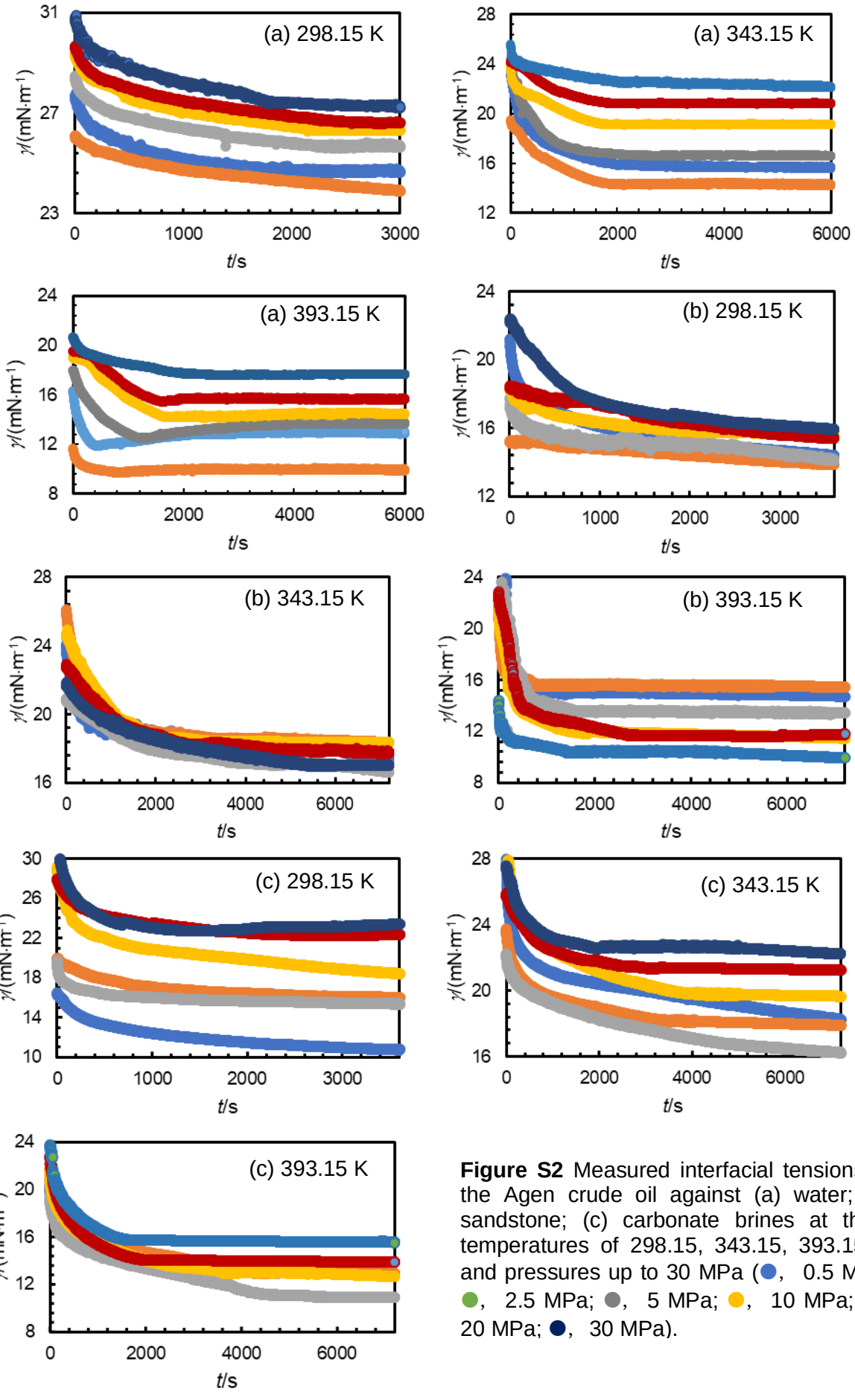

Figure S2 Measured interfacial tensions of the Agen crude oil against (a) water; (b) sandstone; (c) carbonate brines at three temperatures of 298.15, 343.15, 393.15 K and pressures up to 30 MPa (●, 0.5 MPa; ●, 2.5 MPa; ●, 5 MPa; ●, 10 MPa; ●, 20 MPa; ●, 30 MPa).

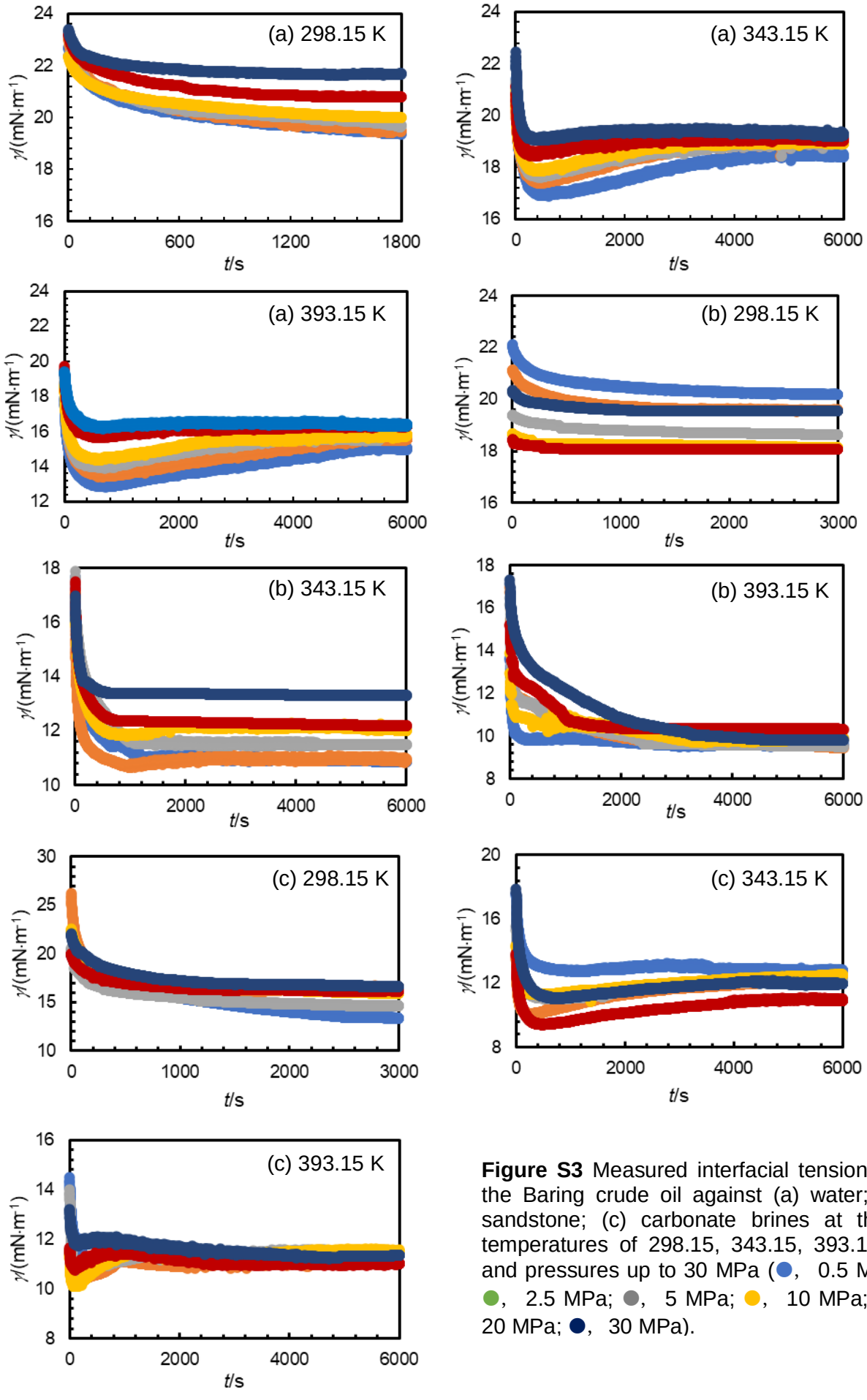

Figure S3 Measured interfacial tensions of the Baring crude oil against (a) water; (b) sandstone; (c) carbonate brines at three temperatures of 298.15, 343.15, 393.15 K and pressures up to 30 MPa (●, 0.5 MPa; ●, 2.5 MPa; ●, 5 MPa; ●, 10 MPa; ●, 20 MPa; ●, 30 MPa).

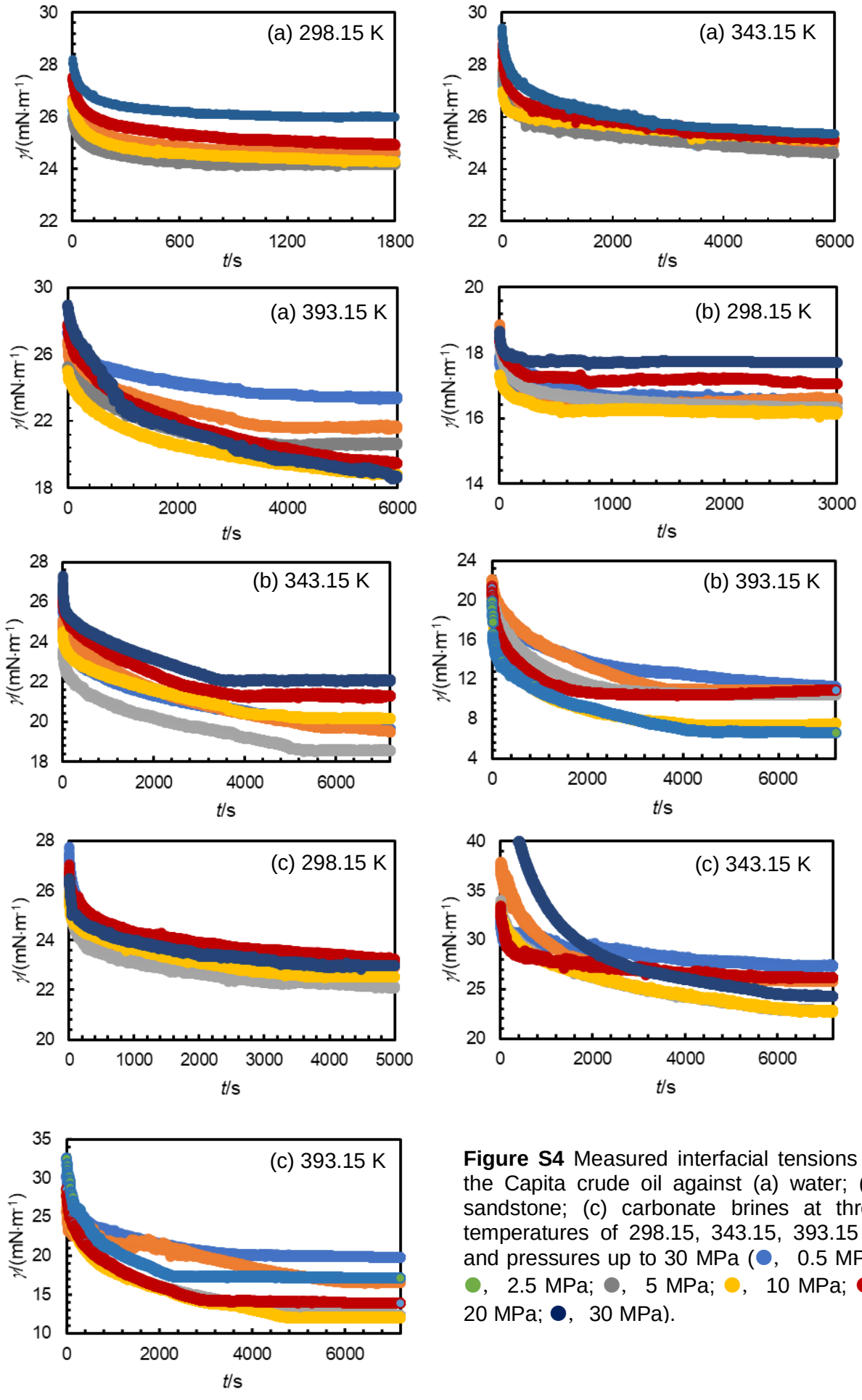

Figure S4 Measured interfacial tensions of the Capita crude oil against (a) water; (b) sandstone; (c) carbonate brines at three temperatures of 298.15, 343.15, 393.15 K and pressures up to 30 MPa (●, 0.5 MPa; ●, 2.5 MPa; ●, 5 MPa; ●, 10 MPa; ●, 20 MPa; ●, 30 MPa).

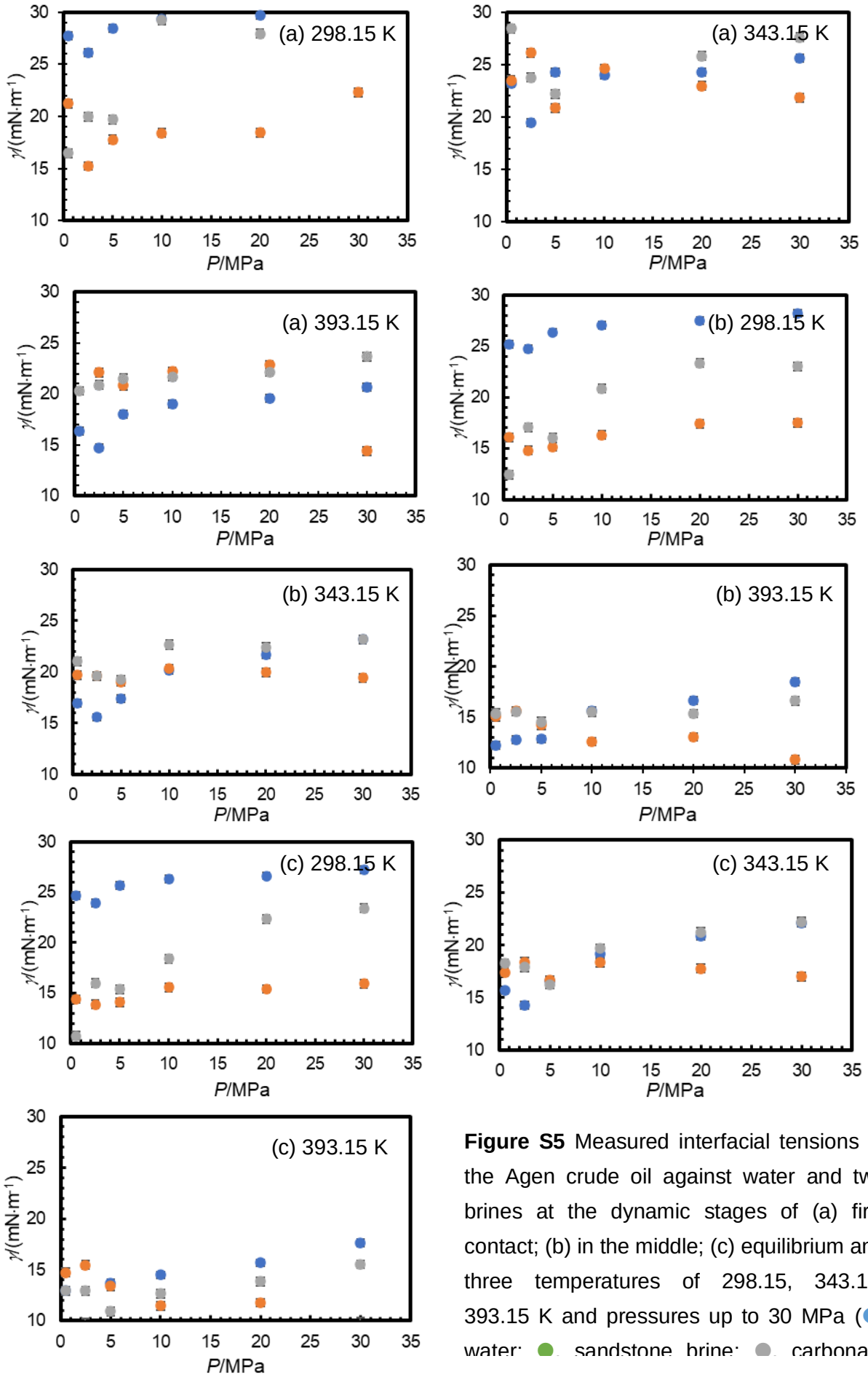

Figure S5 Measured interfacial tensions of the Agen crude oil against water and two brines at the dynamic stages of (a) first contact; (b) in the middle; (c) equilibrium and three temperatures of 298.15, 343.15, 393.15 K and pressures up to 30 MPa (●, water; ● sandstone brine; ● carbonate

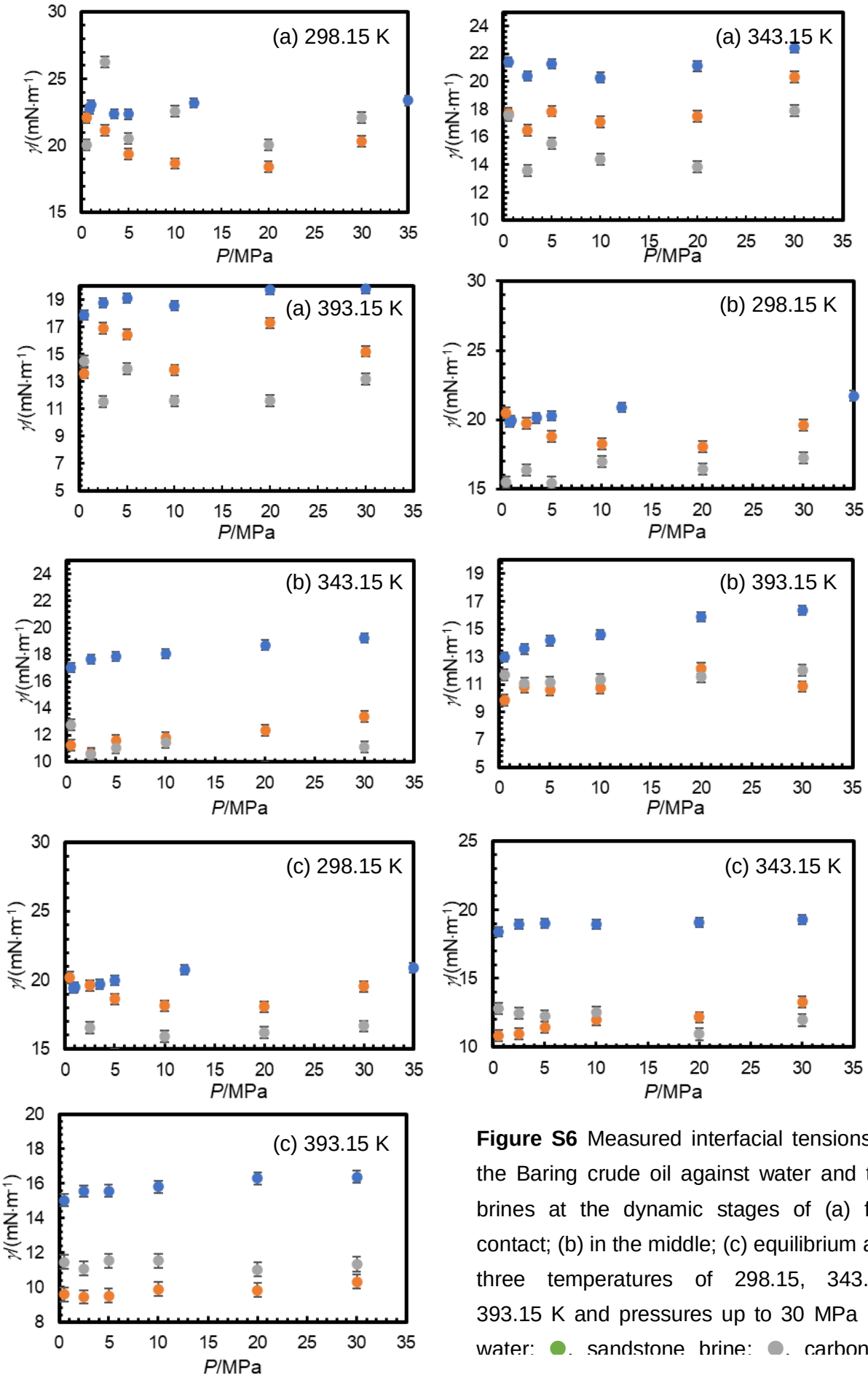

Figure S6 Measured interfacial tensions of the Baring crude oil against water and two brines at the dynamic stages of (a) first contact; (b) in the middle; (c) equilibrium and three temperatures of 298.15, 343.15, 393.15 K and pressures up to 30 MPa (●, water; ●, sandstone brine; ●, carbonate

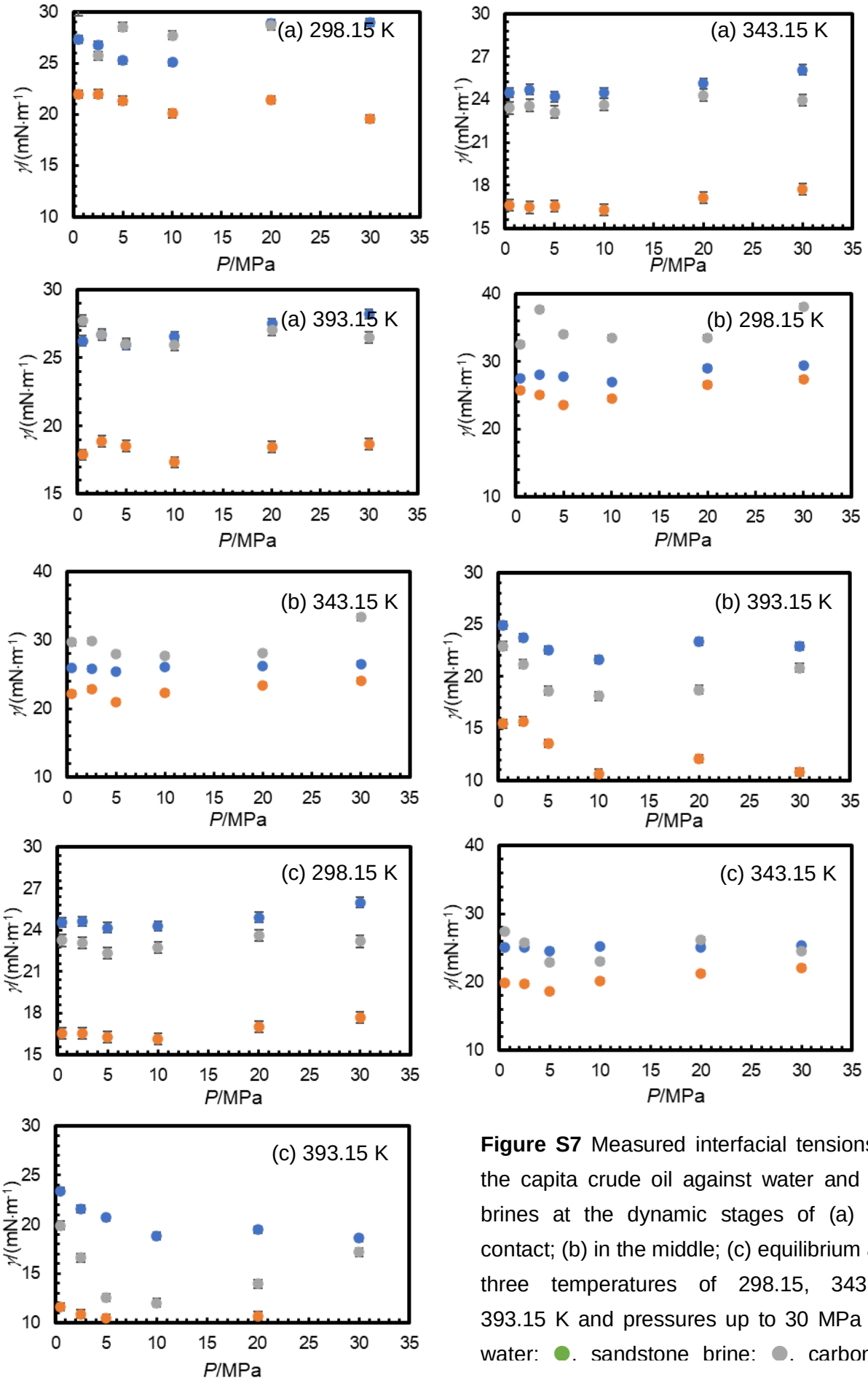

Figure S7 Measured interfacial tensions of the capita crude oil against water and two brines at the dynamic stages of (a) first contact; (b) in the middle; (c) equilibrium and three temperatures of 298.15, 343.15, 393.15 K and pressures up to 30 MPa (●, water; ●, sandstone brine; ●, carbonate

References

[1] Fick A. V. On liquid diffusion. London, Edinburgh, Dublin Philos Mag J Sci 1855;10:30–9.
[2] Sutherland KL. The kinetics of adsorption at liquid surfaces. Aust J Chem 1952;5:683–96.